Quaternary Science Reviews 389 (2026) 110139

Contents lists available at ScienceDirect

Quaternary Science Reviews

journal homepage: www.elsevier.com/locate/quascirev

The deglaciation history of Cape Norton Shaw Inlet (eastern Canadian Arctic Archipelago)

Elodie Bracquart [a,*], Jean-Carlos Montero-Serrano [a,b], Patrick Lajeunesse [c], Guillaume St-Onge [a], Luke Copland [d], Andrew K Hamilton [e], Gabriel Joyal [f]

[a] Institut des Sciences de la mer (ISMER), Université du Québec à Rimouski (UQAR), Geotop & Québec-Océan, Rimouski, QC, Canada
[b] Atmosphere and Ocean Research Institute (AORI), The University of Tokyo, Kashiwa, Chiba, Japan
[c] Département de Géographie, Université Laval & Québec-Océan, Québec, QC, Canada
[d] Department of Geography, Environment and Geomatics, University of Ottawa, Ottawa, ON, Canada
[e] Department of Earth and Atmospheric Sciences, University of Alberta, Edmonton, AB, Canada
[f] Institut National de la Recherche Scientifique (INRS) & Centre de Géomatique du Québec, Québec, QC, Canada

ARTICLE INFO

Handling Editor: Prof Bethan Davies

Keywords:
Glacier dynamics
Submarine landforms
Swath bathymetry
Sediment cores
Ellesmere island
Holocene

ABSTRACT

This study presents a geophysical and morphosedimentary framework for the reconstruction of the glacial history of a fjord of Ellesmere Island, the Cape Norton Shaw Inlet. The reconstruction is based on a multimethod approach combining high-resolution swath bathymetry, acoustic sub-bottom profiles, and a dated composite sediment sequence (33BC/05GGC: 01CNS). The presence of at least five grounding-zone wedges and a large cluster of moraines at the inlet entrance suggests a period of glacial stillstands and gradual retreat during the Younger Dryas. A radiocarbon date of 10.4 cal ka BP from the mid-inlet provides a minimum age for the retreat of the Innuitian Ice Sheet during the early Holocene. Mineralogical and geochemical signatures from core 01CNS, along with low sedimentation rate, support the hypothesis of the gradual opening of Nares Strait between 9.6 and 8 cal ka BP. Until 1.9 cal ka BP, coarse-grained sediments rich in plagioclase and K-feldspar suggest a landward retreat of glaciers bordering the inlet. A dense cluster of recessional moraines suggests a readvance into the inlet of Cape Norton Shaw glaciers during the Little Ice Age, when they reached their Holocene maximum extent. Near the modern glacier front, submarine landforms (including mega-scale glacial lineations, crevasse-squeeze ridges, eskers, terminal moraines and retreat moraines) form a complete surge-type assemblage, confirming the surge behavior of Cape Norton Shaw Glacier. The close correspondence between the terminal moraine position and the 1959 CE glacier front indicates that the most recent surge began around 1959 CE, with the glacier reaching its maximum extent between 1959 and 1971 CE.

1. Introduction

In 2011-2020, the mean global surface temperature reached 1.1°C above the 1850-1900 baseline (IPCC, 2023). Although warm periods comparable to the present have occurred in the past, the current rate of warming is unprecedented. This rapid warming has led to dramatic reductions in sea ice and widespread glacier retreat around the world, especially in the Arctic (e.g., Serreze and Barry, 2011; Sharp et al., 2011; Cohen et al., 2014; Huang et al., 2017; Geyman et al., 2022; IPCC, 2023). Historically, climate fluctuations prior to the industrial era were driven by natural factors such as variations in summer insolation, volcanic eruptions, and solar activity (Ruddiman, 2001; Kaufman et al., 2009; Trujillo and Thurman, 2017). In contrast, the modern-day warming trend is primarily attributed to anthropogenic greenhouse gas emissions (IPCC, 2023). In the Arctic, the phenomenon of Arctic amplification (enhanced recent warming of the atmosphere at high latitudes) has resulted in warming rates up to four times higher than the global average, with some regions experiencing temperature increases exceeding 4°C over the past ~30 years (e.g., Serreze and Barry, 2011; IPCC, 2023; Rantanen et al., 2022).

Within the Arctic, excluding the Greenland Ice Sheet (GrIS), the Canadian Arctic Archipelago (CAA) contains the largest area of land ice, with ice caps and icefields covering over 100,000 km^2 (Sharp et al., 2014). Nearly 300 tidewater glaciers are found in the CAA (Kochtitzky

* Corresponding author.
E-mail address: elodie.bracquart@gmail.com (E. Bracquart).

https://doi.org/10.1016/j.quascirev.2026.110139
Received 5 April 2026; Received in revised form 21 June 2026; Accepted 22 June 2026
Available online 27 June 2026
0277-3791/© 2026 The Authors. Published by Elsevier Ltd. This is an open access article under the CC BY license (http://creativecommons.org/licenses/by/4.0/).

and Copland, 2022). Due to their direct contact with the ocean, tidewater glaciers are more sensitive to environmental change than land-terminating glaciers, as they are influenced by both atmospheric and oceanic conditions (Noël et al., 2018; Cook et al., 2019). Although direct oceanographic observations are limited in the CAA, studies from Greenland indicate that ocean thermal forcing can significantly enhance submarine melting and glacier retreat (Straneo et al., 2010; Jackson et al., 2021). In Nares Strait region, ice arches variability and the North Water Polynya can influence local ocean circulation and heat transport, which may affect tidewater glacier melting in the CAA (e.g., Mundy et al., 2009; Jackson et al., 2021). The GlaMBIE Team (2025) estimated that CAA glaciers have contributed 2.02 ± 0.17 mm to global sea level rise since the beginning of the 21st century (2000-2023). Even under the most optimistic scenarios, where global temperature increase is limited to +1.5°C, glaciers are expected to continue retreating, with projections indicating that nearly half of the world's glaciers, including some in the CAA, could disappear by 2100 (Rounce et al., 2023). In this context, reconstructing paleo-ice sheets and past glacier dynamics is essential for understanding the long-term response and vulnerability of ice masses in the CAA to ongoing and future environmental changes.

Since the 1970s, a series of Earth-observing satellite missions have significantly improved our understanding of glacier responses to modern global warming, such as changes in ice velocity, surface elevation, mass balance, and retreat rates (e.g., Millan et al., 2017; Van Wychen et al., 2020, 2022; Lauzon et al., 2023; Copland et al., 2024). However, studies focusing on paleo-ice sheets and long-term glacier dynamics remain limited and have primarily concentrated on western Greenland and Baffin Island fjords (e.g., Brouard and Lajeunesse, 2019a, 2019b; Funder et al., 2021; O'Regan et al., 2021; Jennings et al., 2022; Couette et al., 2022; Batchelor et al., 2024; Belko et al., 2025). Due to significant logistical challenges, such as persistent heavy sea-ice conditions, that hinder access to remote coastal regions of Ellesmere Island, only a

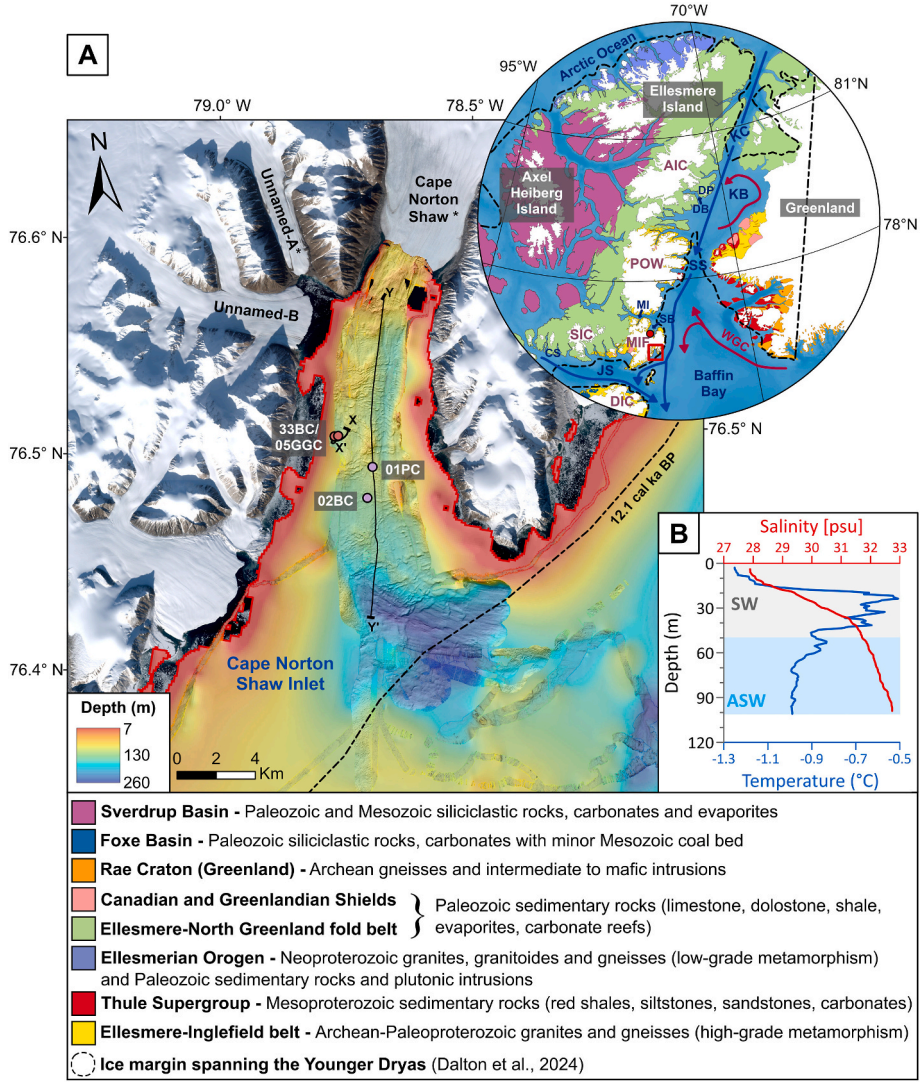

Fig. 1. (A) Map of Cape Norton Shaw Inlet. A Sentinel-2 image acquired on 14 September 2023 (Copernicus.eu) is overlain by the IBCAO topobathymetric map (Jakobsson et al., 2020) and swath bathymetric data collected by the CCGS *Amundsen* and the S/Y *Vagabond*. Cross-profiles X-X′ and Y-Y′ are presented in Fig. 5. The cores studied or cited in this paper are marked by circles: red for 33BC = AMD2303-33BC and 05GGC = AMD2303-05GGC, and purple for 02BC = AMD1803-02BC and 01 PC = AMD1803-01 PC (Stevenard et al., 2022); Asterisks (*) identify surge-type glaciers. The circular map shows the geological setting of northern Baffin Bay and the major surface currents (Harrison et al., 2015). The red arrows represent warm surface currents (>2°C), and the blue arrows represent cold Arctic Surface Water (ASW) (<-1°C). Dashed line indicates the Younger Dryas (~12.1 cal ka BP) optimal ice margin (Dalton et al., 2024). Red circle represents Mittie Glacier. WGC = West Greenland Current; CS=Cape Storm; DB = Dobbin Bay; DP = Darling Peninsula; JS = Jones Sound; KB=Kane Basin; KC=Kennedy Channel; MI = Makinson Inlet; SB=Smith Bay; SS=Smith Sound; AIC=Agassiz Ice Cap; DIC = Devon Ice Cap; MIF = Manson Icefield; POW= Prince of Wales Icefield; SIC=Sydkap Ice Cap. **(B)** Temperature and salinity profiles from CTD casts taken during the 2023 Amundsen expedition at the core locations of 33BC-05GGC (24.09.2023). SW: Surface Water and ASW: Arctic Surface Water. (For interpretation of the references to color in this figure legend, the reader is referred to the Web version of this article.)

limited number of studies have addressed paleoclimate and paleo-environmental reconstructions there since the last deglaciation (e.g., Chassiot et al., 2024; Stevenard et al., 2022; Bracquart et al., 2025). Sediment-landform assemblages, along with their spatial configuration and sedimentological structures, are preserved on the seafloor near glacier margins (e.g., Dowdeswell et al., 2016). The geomorphological record provides valuable archives of past glacier dynamics and can be used to reconstruct their responses to climatic and oceanographic drivers over time (e.g., Streuff et al., 2015; Dowdeswell et al., 2016; Ottesen et al., 2017; Dowdeswell and Ottesen, 2024).

This paper aims at reconstructing the glacial history of Cape Norton Shaw Inlet, a fjord in southeastern Ellesmere Island bordering northwestern Baffin Bay, since the Younger Dryas period (12.9–11.7 cal ka BP; Briner et al., 2009), using a combination of high-resolution swath bathymetry, acoustic sub-bottom profiles, and sediment core data (Figs. 1 and 5 and Figs. 5 and 7). The inlet provides an ideal setting to capture both local variations in glacial sediment discharge from the nearby glaciers and broader regional signals from northern Baffin Bay, extending beyond the instrumental record. Specifically, the objectives of this study are to: 1) reconstruct the retreat history and dynamics of the Innuitian Ice Sheet (IIS) margin and associated glacier systems in Cape Norton Shaw Inlet since the Younger Dryas; 2) assess the influence of climatic and oceanographic changes on glacier dynamics and sedimentation patterns in the inlet throughout the Holocene, including the impact of warming events, sea-ice variability, and the opening of Nares Strait; 3) characterize the sedimentary and geomorphological signatures of surge-type glacier behavior, particularly focusing on Cape Norton Shaw Glacier.

2. Regional settings

Cape Norton Shaw Inlet is located along the eastern margin of Manson Icefield, a ~6000 km^2 icefield on southeast Ellesmere Island (in 1999-2000; RGI 7.0 Consortium, 2023, Fig. 1A). The inlet is ~10 km wide and ~20 km long and surrounded by seven modern tidewater glaciers, as well as former tidewater glaciers that have transitioned to land-terminating positions in recent decades (Kochtitzky and Copland, 2022). Among these glaciers a surge-type glacier (Cape Norton Shaw) and a probable surge-type glacier (Unnamed-A) were identified by Copland et al. (2003). Surge-type glaciers account for only ~1% of the global glacier population and are characterized by cyclical variations, with a long-lived quiescent phase of slow ice flow followed by a short-lived active phase of significantly accelerated ice flow (e.g., Meier and Post, 1969; Raymond, 1987; Dowdeswell et al., 1991; Copland et al., 2003; Sevestre and Benn, 2015). The highest concentration of surge-type glaciers in the CAA (~12%) is found on the north and east sides of Manson Icefield (Copland et al., 2003, 2024). Cape Norton Shaw Glacier is believed to have surged in approximately 1959, as evidenced by widespread crevassing at its front and a looped moraine visible on its west side in summer 1959 aerial photographs (Fig. S1; Copland et al., 2003). The duration of its active phase is not known because of an absence of aerial photographs or satellite images over the 1959-1974 period. Its quiescent phase is probably very long, as no repeat surge has been observed since 1959. Unnamed-A Glacier is believed to have been surging in 1959 and later in 1999, as evidenced by multiple looped moraines along the glacier margin on 1959 aerial photographs and 1999 satellite images (Copland et al., 2003).

The ice-free areas exposed around the inlet are crystalline shield rocks composed mainly of granite, granitoid, and paragneiss rich in quartz, plagioclase, and K-feldspar (Fig. 1A; Brown, 1972; Harrison et al., 2015). Archean to Paleoproterozoic in age, they are related to the Ellesmere-Inglefield Mobile Belt. The sediments found on the seafloor are derived mainly from glacial erosion of the surrounding land masses through various sedimentary processes, such as ice-rafted debris (IRD), glaciogenic debris flows, meltwater plumes, and turbidity currents (Stevenard et al., 2022).

The relative sea-level history of southern Ellesmere Island during the Holocene is rather well constrained by raised beaches and radiocarbon dating. Key sites include Cape Storm, the Darling Peninsula, Dobbin Bay, and Makinson Inlet (Blake, 1975, 1993; Robertson, 1999). In Makinson Inlet, marine shells indicate seawater entered the western arm by 8.93 ± 100 BP and the northern arm by 7.33 ± 80 BP (Blake, 1975). At Cape Storm and Darling Peninsula, radiocarbon ages from driftwood and marine shells suggest a highstand at 8.5-8.0 ka BP (~90 m asl), followed by emergence marked by ages of 7.5-7.0 ka BP (~80 m asl; Blake, 1993). In Dobbin Bay, Robertson, (1999) reports a marine limit of ~71 m asl (~7.3 ka BP) and lower shorelines at ~33 m (~6.0 ka BP), ~15 m (~4.5 ka BP), and ~4 m (~2.0 ka BP), reflecting progressive postglacial emergence. These data indicate rapid coastal uplift during the early to middle Holocene, with cumulative emergence locally ranging from 100 to 120 m since ~9 ka BP, followed by slower late Holocene uplift, demonstrating that relative sea-level in southern Ellesmere Island is largely controlled by regional glacio-isostatic adjustment (Blake, 1993).

During the Last Glacial Maximum, the CAA was covered by the large IIS, GrIS and Laurentide Ice Sheet (LIS) (Dyke et al., 2002; Dalton et al., 2023). The fjord systems and major marine channels, such as Nares Strait, Smith or Lancaster Sounds, were fully blocked by ice until the retreat of the ice sheets during deglaciation (e.g., Knudsen et al., 2008; Jennings et al., 2011; Pieńkowski et al., 2013; Furze et al., 2018). The abrupt cold and arid phase of the Younger Dryas between 12.9 and 11.7 cal ka BP led to readvances or stabilizations of the ice sheets, allowing the building of moraine systems across Baffin Bay (e.g., Briner et al., 2009; Margreth et al., 2017; Young et al., 2020, 2021). The ice-extent reconstructions from the last glaciation to the early Holocene over the study area remain unclear, as there are no paleoclimate data available spanning this period (Dalton et al., 2024). The establishment of warmer temperatures during the early Holocene (Laskar et al., 2004) promoted extensive ice-margin retreat, leading to the progressive opening of oceanic connections between the Arctic Ocean and Baffin Bay. Beginning with Lancaster Sound at 13.5 cal ka BP (Dalton et al., 2023), deglaciation progressed from Smith Sound at approximately 11.15 to 10.4 cal ka BP, to the simultaneous opening of the Kane and Hall Basins at approximately 9.0 cal ka BP (Jennings et al., 2011; Georgiadis et al., 2018; Caron et al., 2019, 2020). With the separation of the IIS and the GrIS, the final opening occurred in Kennedy Channel between 8.5 and 8.3 cal ka BP (Jennings et al., 2011, 2019; Georgiadis et al., 2018). In Nares Strait, the interval from 5.5 to 3 cal ka BP is marked by the predominance of negative phases of the Arctic Oscillation (Funder et al., 2011), which likely promoted the development of seasonal ice arches in Kane Basin, as evidenced by elevated IP_{25} biomarker fluxes and shifts in benthic foraminiferal assemblages (Georgiadis et al., 2020). Following decreasing insolation, proxy reconstructions reveal gradual cooling in air temperatures during the middle to late Holocene (Marcott et al., 2013), which culminated during the Little Ice Age (~1300-1850 CE; Grove, 1988) and promoted the regrowth of glaciers across northern Baffin Bay (Kaufman et al., 2009; Solomina et al., 2015; Briner et al., 2016). Since the end of the 19th century a global and rapid increase in air temperature, primarily driven by increased anthropogenic emissions of gas and aerosols (IPCC, 2023), has caused a recession of CAA glaciers as well as a reduction in the duration and extent of sea ice cover (e.g., Carr et al., 2013; Noël et al., 2018; Cook et al., 2019; Ciracì et al., 2020; Van Wychen et al., 2020; Kochtitzky and Copland, 2022).

In the study area, summers (June-August) are short and cool, with an average temperature of 2.1°C recorded in Ausuittuq (Grise Fiord) in 2024 (https://climate.weather.gc.ca/). In contrast, the remainder of the year (January-May and September-December) is characterized by cold conditions, with an average temperature for these months of −17.2°C in 2024 (https://climate.weather.gc.ca/). These temperature patterns result in Cape Norton Shaw Inlet typically being covered by sea ice from September to May, with ice breakup usually beginning in June.

The temperature-salinity profile in the study area indicates the

presence of two main water masses, consistent with those identified by Tang et al., 2004 in northern Baffin Bay (Fig. 1B; Amundsen Science, 2023). The Surface Water (SW) occupies the upper layer and is characterized by relatively low salinity that increases with depth (~28-32 PSU), reflecting inputs of glacial meltwater from surrounding glacierized catchments and sea-ice melting, as well as seasonal freshwater discharge from tidewater glaciers. Below, the Arctic Surface Water (ASW) extends from ~50 to 100 m depth and is characterized by colder temperatures (−1 to −0.8°C) and higher salinity (32-33 PSU), reflecting the influence of Arctic Ocean waters transported into northern Baffin Bay.

3. Material and methods

3.1. Swath bathymetry and acoustic stratigraphy

Swath bathymetry data from the inlet and glacier front were collected in 2019 onboard the S/Y *Vagabond* using a R2Sonic Sonic2026 (90–450 kHz) multibeam echosounder (MBES) (Hamilton et al., 2021). A second dataset completing the inlet cover was collected in 2017, 2018 and 2023 onboard the CCGS *Amundsen* using a Kongsberg EM-302 (30 kHz) and an EM-304 (30 kHz) MBES operated with the Seafloor Information System (SIS) (Amundsen Science Data Collection, 2017a; 2018a; 2023a). In 2023, the glacier front was surveyed by the CCGS *Amundsen* barge equipped with a Kongsberg EM-2040 MBES (200-400 kHz). For the four datasets, the raw data were processed with CARIS® Hips and Sips software to correct for anomalous data points, navigation artifacts and tidal effects. The data were gridded at 10 m (inlet-S/Y *Vagabond*), 3 m (inlet-CCGS *Amundsen*), and 1 m (glacier front-CCGS *Amundsen*) grid resolutions for better interpretation and analysis.

The acoustic sub-bottom survey undertaken in 2017, 2018 and 2023 onboard the CCGS Amundsen used a Knudsen 3260 CHIRP sub-bottom profiler with a 3.5 kHz transducer (Amundsen Science Data Collection, 2017b; 2018b; 2023b). Acoustic images of sedimentary units were extracted, processed and interpreted using the National Resources Canada (NRCan) SegyJP2Viewer software (Courtney, 2007), with a sound velocity of 1500 m s^{-1}.

3.2. Sediment coring and analyses

Two sediment cores, AMD2303-33BC and 05GGC (Table 1), were recovered on the western side of Cape Norton Shaw Inlet during the 2023 ArcticNet expedition onboard the Canadian Coast Guard Ship (CCGS) icebreaker *Amundsen*. Coring sites were determined via high-resolution seismic profiles and swath bathymetric data to identify areas with continuous sequences showing no mass movements or sediment disturbance.

Digital X-ray images of the sediment cores were acquired using a GEOTEK X-ray computed tomography (X-CT) system prior to measuring wet bulk density on the whole cores with a GEOTEK Multi-Sensor Core Logger (MSCL), at 0.5 cm intervals for core 33BC and 1 cm intervals for core 05GGC. Following these measurements, the sediment cores were split, visually described, and high-resolution digital color photographs (HRPs) were taken using a GEOTEK Geoscan IV imaging system. Magnetic susceptibility (k_{LF}), diffuse spectral reflectance, and elemental composition were also measured using the MSCL at the same intervals. Sediment color reflectance was obtained with a portable Minolta CM-2600d spectrophotometer integrated into the MSCL, and expressed according in the L* (black to white), a* (green to red), b* (blue to yellow) color space of the International Commission of Light (e.g., St-Onge et al., 2007). Relative elemental concentrations (including Al, Si, Ti, Ca, K, Fe, Mn, Zn, Rb, Sr, and Zr) were determined using a portable Olympus Innov-X DELTA pXRF analyzer, equipped with a 40 kV rhodium anode X-ray tube and integrated with the MSCL. The pXRF analysis was performed using the GeoChem method with two beams (40 and 10 kV) with a 60-s exposure time per beam. Prior to the analysis, 1-cm-wide subsamples were taken at every centimeter for core 33BC and at ~4 cm intervals for core 05GGC.

Grain size analyses (<2 mm fraction) were performed with a *Malvern-Panalytical Mastersizer 3000* particle size analyzer equipped with a HydroLV module following the instrumental conditions outlined in Belzile and Montero-Serrano (2022). Before measurement, the samples were pretreated with 10 mL of hydrogen peroxide (H_2O_2; 30%) to remove organic matter, air-dried under a fume hood, diluted with 20 mL of sodium hexametaphosphate (20% v/v), sieved at <2 mm, and disaggregated using an in-house rotator for 12 h prior to analysis. The grain size composition (clay, silt, and sand) and statistical parameters (D_{90}, sorting) were extracted with *GRADISTAT* software version 9.1 (Blott and Pye, 2001). The mean grain size of the noncohesive silt fraction (10-63 μm), referred to as sortable silt ($\overline{SS}$), along with its proportion within the <63 μm fraction (SS%), was calculated to infer variations in sediment transport driven by near-bottom currents (Fig. S6), following the method outlined by McCave and Andrews (2019a). The abundances of coarse sand (>400 μm) were used to identify layers of the high rafting of coarse material by ice (e.g., ice-rafted debris or IRD and sea-ice transport; Andrews, 2000; McCave and Andrews, 2019a). In addition, the coarse IRDs abundance was quantified by counting gravel clasts >2 mm in size on X-CT scans of cores in contiguous 2-cm windows (Grobe, 1987).

The quantitative X-ray diffraction mineralogy (qXRD) of the <2 mm bulk sediment fraction was analyzed following the method developed by Eberl (2003). The clasts >2 mm found in the ice-rafted debris-rich layers (hereafter referred to as IRD1 to IRD5) were also analyzed, except for IRD4, because of the insufficient quantity of material (Fig. 6B). Sample preparation involved grinding 1 g of dry sediment spiked with 0.25 g of corundum in a McCrone micronizing mill using 5 mL of ethanol for 7 min. The resulting slurry was air-dried, after which 0.25 mL of Vertrel was added to prevent agglomeration of fine particles. The samples were then sieved (<500 μm), backloaded into sample holders, and analyzed using a PANalytical X'Pert Powder diffractometer. The samples were scanned between 5° and 65° two-theta with a step of 0.02° two-theta and a count time of 2 s per step. The quantification was established by converting the intensity data into mineral weight percentages (wt.%) via powdR software (Butler and Hillier, 2021). This fitting method quantifies the mineralogy of a sample with an average absolute bias of 0.6% for nonclay minerals, 2% for clay minerals and 5% for amorphous phases (Omotoso et al., 2006; Butler and Hillier, 2021). The calculated total mineral content (wt.%) was normalized to a sum of 100%. To gain a quantitative understanding of the downcore changes in the bulk sediment provenance, we ran the nonlinear unmixing Excel macro SedUnMix on the normalized data for the principal minerals (Pl, Kfs, Qz, Bt, Chl, Ill, Ms, Sme, Vm, Cal and Dol) that represented more than 85% of the overall mineral concentration in the samples (Andrews and Eberl, 2012; Andrews et al., 2015, 2016).

The chronology of the sediment cores was established using seven accelerator mass spectrometry (AMS) radiocarbon (^{14}C) ages (Table 2), analyzed at the A.E. Lalonde AMS laboratory (University of Ottawa,

Table 1
Summary of core stations studied here. BC = box core; GGC = giant gravity core.

Core ID	Latitude (°N)	Longitude (°W)	Water depth (m)	Core length (cm)	Date of collection (dd-mm-yyyy)
AMD2303-33BC	76.5040	78.7973	129	52	24-09-2023
AMD2303-05GGC	76.5041	78.7903	130	300	24-09-2023

Table 2
Radiocarbon (^{14}C) ages obtained by accelerator mass spectrometry (AMS) for sediment cores 33BC and 05GGC. Calibrated ages were calculated using the rbacon Bayesian age-depth modeling package (Blaauw and Christen, 2011) and the Marine20 calibration curve (Heaton et al., 2020).

Laboratory number	Core	Material	Depth in composite core 01CNS (cm)	^{14}C age uncalibrated (yr BP)	ΔR = 71 ± 69 (cal yr BP)	
					Median probability (cal yr BP)	Range 2σ (cal yr BP)
UOC-25412	33BC	Shell fragment	52	745 ± 15	226	127-352
UOC-25413	05GGC	Shell fragment	60.5-61.5	1150 ± 15	471	298-588
UOC-25414	05GGC	Shell fragment	73-74	1430 ± 15	698	555-856
AWI-13869.1.1	05GGC	Shell fragment	142-143	2269 ± 66	1822	1584-2098
UOC-25415	05GGC	Shell fragment	238	5810 ± 20	5781	5599-5971
UOC-25416	05GGC	Shell fragment	263-264	5910 ± 20	6208	6036-6403
UOC-25417	05GGC	Shell fragment	298	9230 ± 25	9550	9319-9766

Canada) and the Alfred Wegener Institute - Helmholtz Centre for Polar and Marine Research (Bremerhaven, Germany). The ^{14}C ages were calibrated using the Marine20 calibration curve (Heaton et al., 2020), with a local marine reservoir correction (ΔR) of 71 ± 69 years, established for the South Nares Strait region (Pearce et al., 2023). The recent chronology (<150 years) was constrained using ^{210}Pb measurements on dry sediment samples from core 33BC at 1-cm intervals (Table S1). ^{210}Pb measurements were performed at the Geotop research center (Montréal, Canada) by alpha spectrometry. Prior to analysis, samples were sieved through 150-μm Nitex® mesh to minimize grain size-related biases, oven-dried at 60°C, and homogenized by crushing.

Based on the correlation of the ln(Ca/K) and b* profiles, we estimate that ~40 cm of sediment at the top of 05GGC was lost during coring (Fig. S2). Therefore, cores 33BC and 05GGC were combined into a composite sequence: 01CNS (hereafter, only the composite sequence was used). The upper 50 cm of 01CNS corresponds to core 33BC, and the rest of the sequence corresponds to core 05GGC (50–337 cm). The age-depth model was generated using the corrected composite depths.

The Short-Lived Radionuclide Chronology (SERAC) R package and the constant flux constant sedimentation (CFCS) model, assuming no mixing or Pb diffusion in the sediment (Bruel and Sabatier, 2020), were used to construct the ^{210}Pb-based age model for core 33BC (Fig. S3). These results, combined with radiocarbon dating, were then processed via the R package 'rbacon' (version 3.3.1; Blaauw and Christen, 2011) to generate the most robust age−depth model for the composite sequences 01CNS. The rbacon package estimates the best-fit (or weighted mean) age for each depth with a 95% confidence interval using a Bayesian approach.

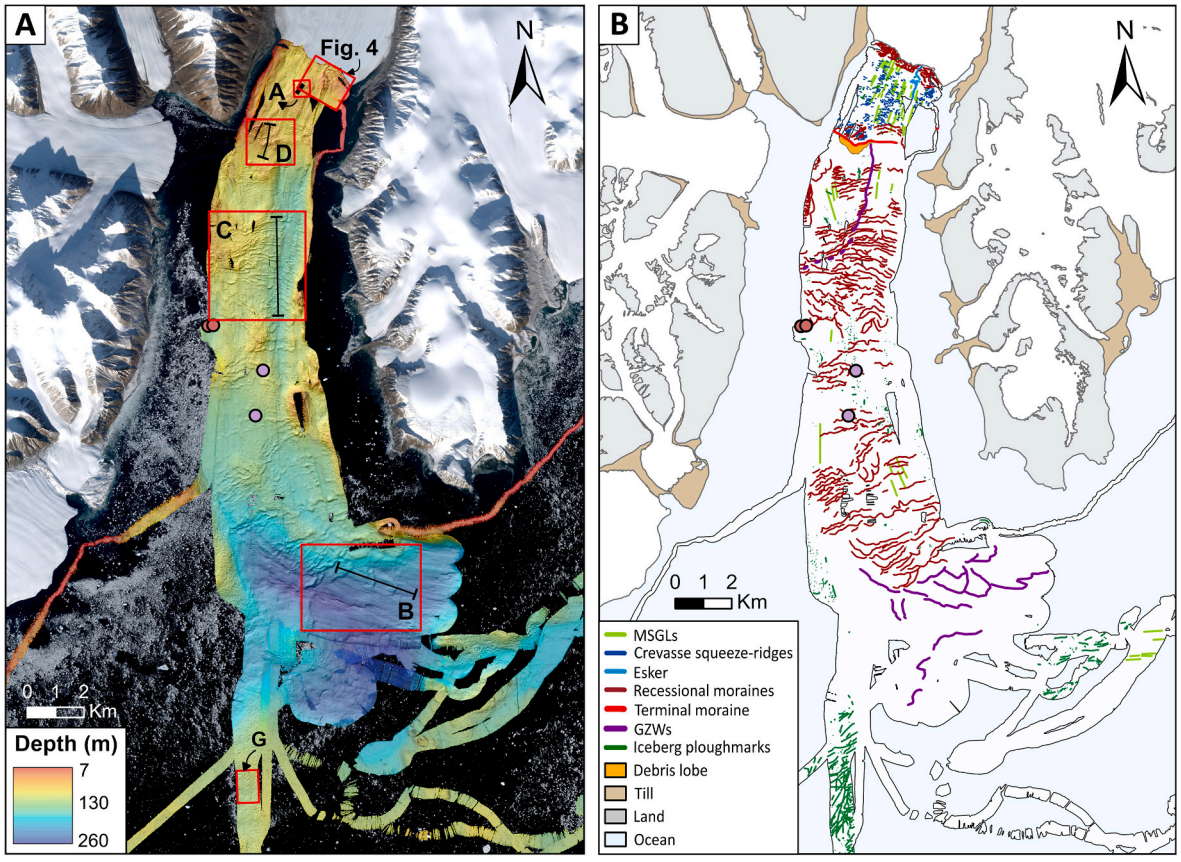

Fig. 2. **(A)** Swath bathymetry and 2023 Sentinel-2 satellite imagery (14/09/2023) of the modern glacier fronts in Cape Norton Shaw Inlet with cross profiles B-B′, C-C′ and D-D'. The red boxes show the locations of Fig. 3A, B, C, D and G close-ups and Fig. 4. The cores studied or cited in this paper are marked by circles: red for 33BC = AMD2303-33BC and 05GGC = AMD2303-05GGC, and purple for 02BC = AMD1803-02BC and 01 PC = AMD1803-01 PC (Stevenard et al., 2022). **(B)** Interpreted submarine landform distribution across the inlet. The color code follows the GlaciDat database from Streuff et al. (2022). (For interpretation of the references to color in this figure legend, the reader is referred to the Web version of this article.)

4. Results and interpretations

4.1. Submarine landform assemblage

Swath bathymetric imagery from Cape Norton Shaw Glacier front to the entrance of the inlet revealed an asymmetric seafloor overprinted by well-preserved landforms (Fig. 2). The inlet is relatively shallow with a maximum depth of 260 m at the entrance (Fig. 1A). No evidence of a sill restricting exchange of deeper waters with offshore was found at the entrance of the inlet. The submarine landforms overprinting the seafloor indicate that Cape Norton Shaw Inlet was occupied by an ice stream that extended into northern Baffin Bay. The landforms were mapped and regrouped under three environments (Fig. 2B): subglacial (mega-scale glacial lineations or MSGL, crevasse-squeeze ridges or CSR, and eskers), ice-marginal (grounding-zone wedges or GZW, terminal and recessional moraine ridges) and glaciomarine (iceberg ploughmarks).

4.1.1. Subglacial environment

The three landforms described below are observed only between the Cape Norton Shaw Glacier front and the terminal moraine described in section 4.1.2.

Mega-scale glacial lineations. - Several positive landforms aligned with the inlet topography and oriented NNE–SSW are observed near Cape Norton Shaw Glacier front (Fig. 2and Fig. 3A). These elongated ridges are parallel to subparallel to each other and measure 40–80 m in width, 400–1000 m in length, and approximately 4 m in height. Their elongation ratios (1:10) and overall metrics are consistent with those of mega-scale glacial lineations, although they fall at the lower end of the length range reported for this type of landform (e.g., Spagnolo et al., 2014; Brouard and Lajeunesse, 2019a, 2019b; Couette et al., 2023; Belko et al., 2025). Comparable features have been documented in fjords and cross-shelf trough systems off Baffin Island, including ridges up to 7.1 km long and ~390 m wide (Brouard and Lajeunesse, 2019a, 2019b), as well as ridges 50–500 m wide and up to 5 km long (Couette et al., 2023), and ridges 50–300 m wide, 2–4 km long, and less than 10 m high (Belko et al., 2025). Recognized across various regions of the Arctic, mega-scale glacial lineations are commonly produced subglacially by soft glaciogenic sediment deformation at the glacier-bed interface. They are associated with fast ice flow, such as grounded ice streams or surging glaciers, and their orientation provides an indicator of former ice-flow direction (e.g., Clark, 1993; Dowdeswell et al., 2008; Spagnolo et al., 2016; Ottesen et al., 2017; Brouard and Lajeunesse, 2019a, 2019b; Couette et al., 2023; Belko et al., 2025). The presence of these mega-scale glacial lineations indicates that Cape Norton Shaw Glacier experienced a rather recent episode of rapid advance.

Crevasse-squeeze ridges. - Swarms of small sharp-crested ridges broadly oriented transverse to ice flows are found in association with the mega-scale glacial lineations (Fig. 2and Fig. 3A). These ridges are linear, parallel to subparallel, and occasionally form a distinctive rhombohedral pattern. They are relatively small, with heights of 4–8 m, widths up to 20 m, and lengths typically <100 m. The morphology of these landforms is typical of crevasse-squeeze ridges (Sharp, 1985; Evans and Rea, 1999). Recognized worldwide in submarine and terrestrial settings, crevasse-squeeze ridges have been historically associated with surge-type glacier behaviors (e.g., Sharp, 1985; Evans and Rea, 1999; Ottesen et al., 2008; Streuff et al., 2015; Ingólfsson et al., 2016; Ben-Yehoshua et al., 2023; Osika and Jania, 2024). Crevasse-squeeze ridges are produced during initial post-surge ice stagnation by soft subglacial sediments squeezed upward into bottom-up crevasses when the basal water pressure decreases under the weight of overlying ice (Ottesen and Dowdeswell, 2006; Ottesen et al., 2008). More recently, Crevasse-squeeze ridges have been identified on paleo-ice stream beds and are associated with the final stages of ice streaming and deglaciation (Evans et al., 2016; Kurjanski et al., 2019). The presence of multiple crevasse-squeeze ridges close to Cape Norton Shaw Glacier front indicates a past heavy crevassed front.

Eskers. – A single sinuous, sharp-crested, and discontinuous ridge, approximately 1.5 km long, ~100 m wide, and 10-20 m high, originates close to the present-day grounded ice front (Fig. 2andFig. 4). This ridge is interpreted as an esker formed near the ice margin through the accumulation of gravel and sandy sediments deposited by meltwater flowing within a subglacial R-channel (e.g., Röthlisberger, 1972; Banerjee and McDonald, 1975; Brennand, 2000; Dowdeswell and Ottesen, 2016; Lajeunesse, 2016. The esker therefore records the former position of a subglacial meltwater channel beneath Cape Norton Shaw Glacier.

The short and discontinuous shape of the esker could be explained by several factors (Brennand, 2000 and references therein). However, given its association with landforms diagnostic of surge-type glacier activity preserved in the morpho-sedimentary record (e.g., mega-scale glacial lineations, crevasse-squeeze ridges, recessional and terminal moraines), the esker was most likely formed under active ice during a surge of Cape Norton Shaw Glacier (Brennand, 2000; Evans and Rea, 2003; Ottesen et al., 2008). In a surge-type glacier setting, the instability of the subglacial drainage system plays a key role: rapid ice flow and elevated basal water pressure promote frequent reorganization of meltwater pathways (Röthlisberger, 1972). This mechanism limits the long-term stability and persistence of R-channels and promotes the development of short discontinuous eskers instead of long continuous ridge systems.

During the 2019 *Vagabond* and 2023 CCGS *Amundsen* expeditions, a subglacial meltwater tunnel at the glacier front (Fig. 4B) and a sediment plume (18/08/2023) were observed near the head of the esker, supporting the interpretation of active or recent subglacial meltwater discharge in this area.

4.1.2. Ice-marginal environment

Grounding-zone wedges. – At least four low-amplitude, asymmetric wedges with sinuous crestlines are observed at the entrance of the inlet at water depth of 180–210 m (Fig. 2andFig. 3B). These small wedges are ~300–650 m long in the former ice-flow direction, ~1–3 km wide, and up to 10 m high, with gently dipping ice-proximal flanks and steeper ice-distal flanks. A larger asymmetric wedge, overprinted by recessional moraines, occurs in the inner inlet in front of Unnamed-B Glacier. This wedge is at least 1.5 km long, ~5 km wide, and up to 30 m high, with a minimum area extent of ~8 km^2. These asymmetric wedges are interpreted as grounding-zone wedges. In the absence of exploitable sub-bottom data (Fig. 5A), they are distinguished from recessional moraines by their low-amplitude morphology and steeper ice-distal flanks. Compared to 3-50 km long grounding-zone wedges observed in the CAA on Beaufort Sea margins (Batchelor and Dowdeswell, 2015) and Baffin Island shelves (Brouard and Lajeunesse, 2019a; Couette et al., 2023; Belko et al., 2025), those in Cape Norton Shaw Inlet are relatively small. This apparent size difference likely reflects a preservation bias, as the full extent of the grounding-zone wedges may be masked by the stacking of successive wedges and by recessional moraine ridges, which together hinder the recognition of their maximum original dimensions.

Grounding-zone wedges form through the delivery of deformable subglacial sediments where ice margins cease to be in contact with the bed during stillstands and thus record former grounding-line positions (Dowdeswell et al., 2008; Ottesen and Dowdeswell, 2009; Dowdeswell and Fugelli, 2012; Batchelor and Dowdeswell, 2015; Lajeunesse et al., 2019a). They are typically found in fjords occupied by fast-flowing ice streams, marine-terminating glaciers and ice sheets located at high latitudes in the Arctic (Brouard and Lajeunesse, 2019a, 2019b; Couette et al., 2023; Belko et al., 2025) and Antarctic regions (Dowdeswell et al., 2008; Simkins et al., 2018), as well as on previously glaciated continental shelves (Batchelor and Dowdeswell, 2015; Lajeunesse et al., 2019). In Cape Norton Shaw Inlet, the cluster of grounding-zone wedges at the entrance suggests that the ice margin once extended into Baffin Bay, with its retreat punctuated by multiple relatively short-lived stillstands or minor readvances of the grounding zone, likely during the last deglaciation. In contrast, the larger grounding-zone wedge in the inner

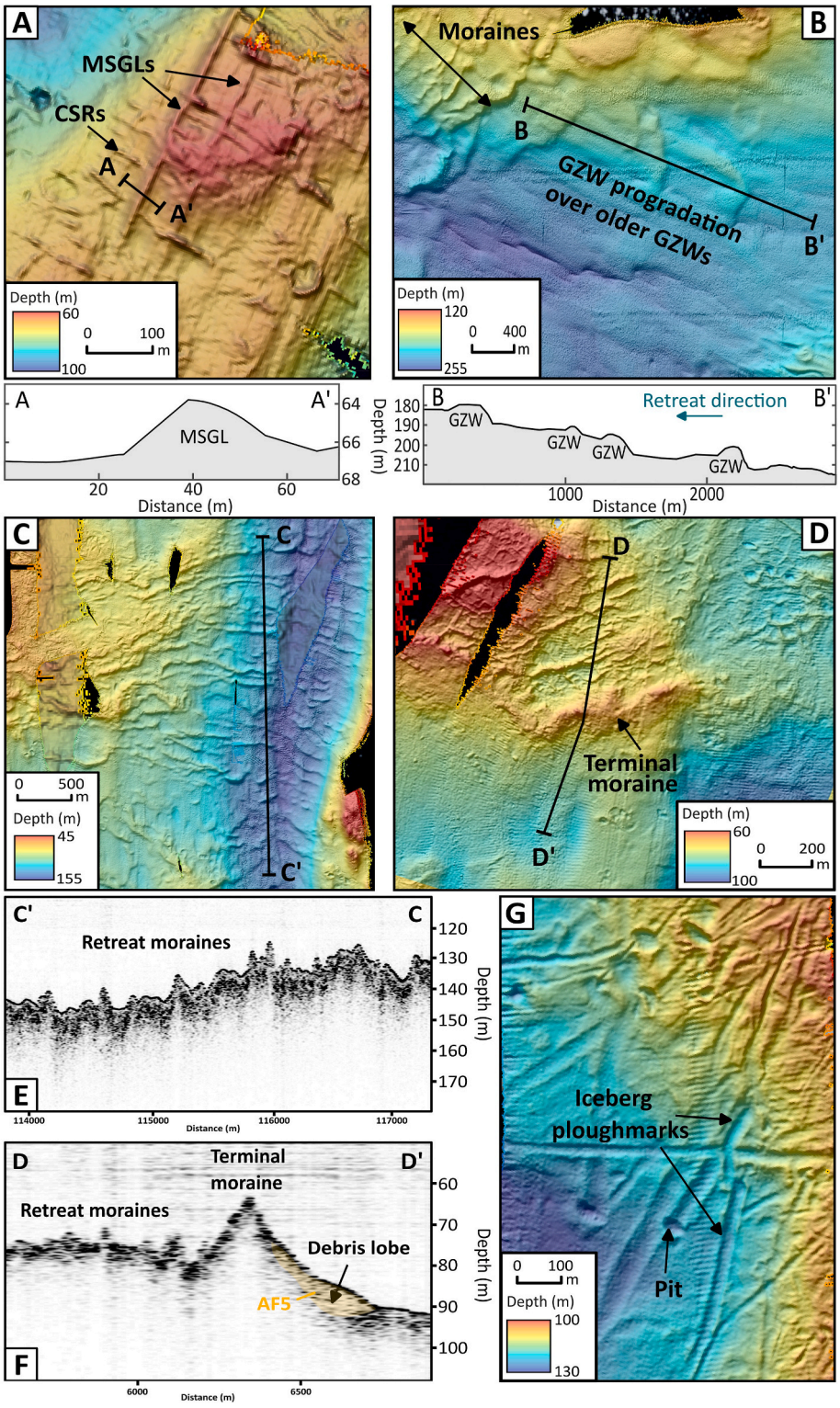

Fig. 3. Close-ups of submarine landforms in Cape Norton Shaw Inlet. **(A)** Examples of mega-scale glacial lineations (MSGLs) and crevasse squeeze-ridges (CSRs) landforms and cross-section profile A-A′ across a mega-scale glacial lineation. **(B)** Examples of grounding zone wedges (GZW) and retreat moraine landforms with cross-section profile B-B′ across prograding grounding zone wedges. **(C)** Examples of De Geer moraines with the cross-section profile C-C′ associated with the seismic profile **(E)**. **(D)** Examples of the 1959 terminal moraine, debris lobe and De Geer moraines with cross-sectional profile D-D′ associated with the seismic profile **(F)**. **(G)** Examples of iceberg ploughmarks and pits at the mouth of the inlet. (For interpretation of the references to color in this figure legend, the reader is referred to the Web version of this article.)

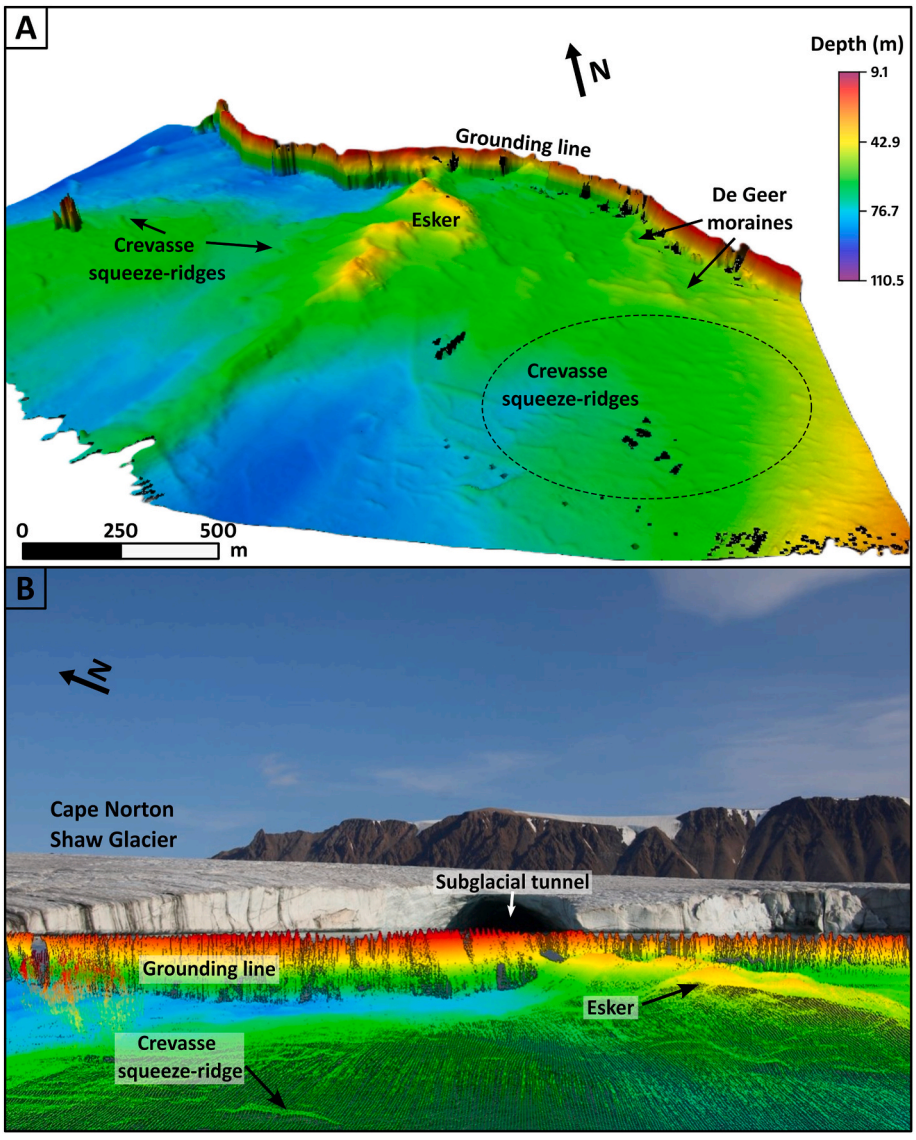

Fig. 4. **(A)** Bathymetric surface of an esker located close to the modern Cape Norton Shaw Glacier front with swarms of crevasse squeeze-ridges on both sides. **(B)** Photograph of the 2019 Cape Norton Shaw Glacier front showing the spatial relationship between the tunnel and the position of the esker in 2019. Location of the figure is provided on Fig. 2A. (For interpretation of the references to color in this figure legend, the reader is referred to the Web version of this article.)

inlet, located in front of Unnamed-B Glacier, records a distinct period of grounding-line stabilization that postdates the formation of the outer grounding-zone wedges.

Recessional moraine ridges. - Five clusters of low-amplitude, long, narrow, and elongated ridges are observed across the inlet (Fig. 2and Fig. 3C). These ridges are generally parallel to sub-parallel and oriented transverse to the former ice-flow direction. In the inner inlet, two distinct clusters are identified: one comprising ~10 ridges adjacent to the modern Cape Norton Shaw Glacier front, and another consisting of 3–4 ridges located approximately 2 km farther offshore. In this area, ridge spacing averages ~30 m, with lengths ranging from tens of m to ~500 m and an average height of ~3 m. In the central part of the inlet, a first set of ~8 ridges is overlain by a second denser cluster of 30-40 ridges. Here, the ridges are generally more continuous, with average lengths of ~650 m and heights of ~5 m. At the entrance of the inlet, 25-28 ridges are less well defined and appear partially eroded. In this area, spacing increases to ~90 m, with individual ridges measuring ~2 m in length and ~4 m in height.

On sub-bottom profiles, the ridges are clearly identifiable by their sawtooth morphology and (semi-)transparent, acoustically massive reflections, suggesting a mixed lithological composition of glaciogenic origin (Figs. 3E and 5). These ridges are interpreted as recessional moraines or De Geer moraines (De Geer, 1889). Such landforms typically form annually through sediment squeezing and push processes during minor winter readvances of the glacier terminus under overall retreat conditions (Boulton, 1986; Ottesen and Dowdeswell, 2006, 2009; Dowdeswell et al., 2008; Benn and Evans, 2010; Brouard and Lajeunesse, 2019a, 2019b; Couette et al., 2023). The five distinct clusters of moraines indicate at least five periods of overall grounding-line retreat in Cape Norton Shaw Inlet.

Terminal moraine ridge and debris lobe. – A single large transverse ridge is observed in the inner part of the inlet, extending laterally toward the right margin, where it emerges above sea level and transitions into an aerial landform (Fig. 2andFig. 3D). The submerged section of the ridge, ~20 m in height and ~350 m in width, is characterized by a steep proximal flank and a more gently sloping distal flank. Similar to the recessional moraines, the ridge displays (semi-) transparent and acoustically massive reflections, indicative of a mixed lithological composition dominated by glaciogenic sediments (Fig. 3F). This landform is interpreted as a terminal moraine formed either during a glacier

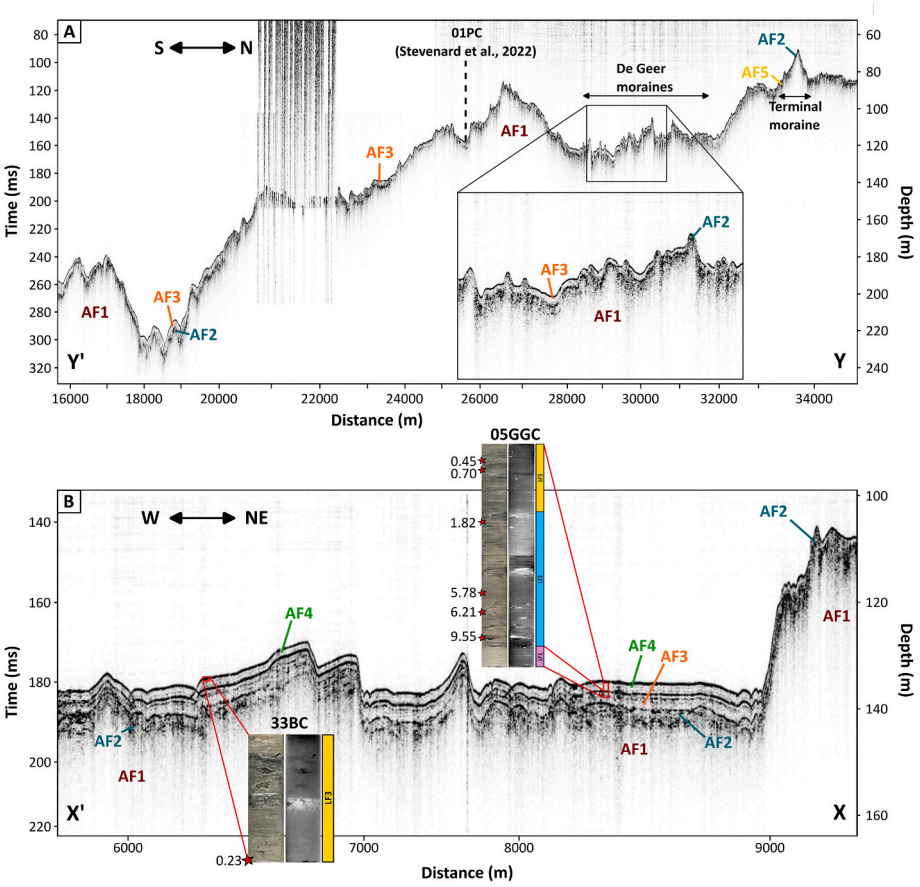

Fig. 5. Acoustic sub-bottom profiles across Cape Norton Shaw Inlet with interpreted units. The locations of the profiles are shown in Fig. 1. **(A)** Sub-bottom profile Y′-Y of lines 211-0957 acquired in 2017, showing the approximate locations of core 01 PC (Stevenard et al., 2022) and four acoustic facies (AF1-AF3 and AF5). **(B)** Sub-bottom profile X′-X of lines 267-1412 acquired in 2023, showing the approximate locations of cores 33BC and 05GGC and the acoustic facies AF1-AF4. The red stars in the figure indicate ages in cal yr BP. (For interpretation of the references to color in this figure legend, the reader is referred to the Web version of this article.)

advance or at the maximum extent of a surge event (e.g., Benn and Evans, 2010; Dowdeswell et al., 2016; Couette et al., 2023). No other large submarine moraine landforms were observed farther offshore. The presence of typical surge-related landforms (mega-scale glacial lineations, crevasse-squeeze ridges, esker, recessional moraines) between the present-day glacier front and the terminal moraine suggests that this ridge is probably associated with a surge event. Moreover, its position closely matches the front location of Cape Norton Shaw Glacier on satellite imagery from summer 1959 (Fig. S1), suggesting that the moraine marks the maximum extent reached during the ~1959 surge. A small lobe-shaped deposit is visible downslope of the distal flank of the terminal moraine (Fig. 3F). This lobe reaches ~500 m in width and ~200 m in downslope length. This deposit is interpreted as a glaciogenic debris flow, likely resulting from the rapid release and failure of soft subglacial sediments at the former ice front of Cape Norton Shaw Glacier during the ~1959 surge (Couette et al., 2023).

4.1.3. Glacimarine environment

Iceberg ploughmarks. - The inlet seafloor is incised by linear to curvilinear grooves, mostly located at the entrance of the Inlet to a maximum depth of 160 m (Fig. 2). These landforms are relatively long and narrow, in some cases terminating in pits, and are typically less than 800 m in length, 10 to 60 m width, and a few meters deep. Their distribution is highly irregular, with straight segments interspersed with directional shifts and abrupt changes in orientation (Fig. 3G). The variety of patterns and morphologies observed is similar to those described as resulting from drifting iceberg keels scouring seafloor sediments after calving from a marine-based glacier or ice-sheet terminus (e.g., Woodworth-Lynas et al., 1985; Syvitski et al., 2001; Dowdeswell and Ottesen, 2013; Dowdeswell et al., 2016; Gales et al., 2016; Brouard and Lajeunesse, 2019b; Couette et al., 2023); these landforms are therefore interpreted as iceberg ploughmarks. In addition, small individual, sub-rounded to rounded pits are observed (Fig. 3G). These landforms are randomly distributed across the inlet, extending into shallow waters at depths <200 m. The depressions are less than 5 m deep and range in diameter from tens to hundreds of meters. These pits are probably the result of intermittent contact between iceberg keels and the sedimentary seafloor, occurring as icebergs adjust their hydrostatic equilibrium during melting or in response to changes in water depth (Syvitski et al., 2001). Iceberg ploughmarks and pits are widely recognized across many areas of the Arctic continental margins (e.g., Dowdeswell et al., 2010, 2016; Bjarnadóttir et al., 2016; Jakobsson and O'Regan, 2016; Montelli et al., 2018; Brouard and Lajeunesse, 2019b; Couette et al., 2023; Dowdeswell and Ottesen, 2024).

4.2. Sub-bottom acoustic stratigraphy

From the 2017 and 2023 surveys of Cape Norton Shaw Inlet (Fig. 5), five acoustic facies (AF1-AF5) were differentiated based on their acoustic signatures, bounding reflectors and internal geometries. Their characteristics are summarized in Table 3.

The **AF1** facies is acoustically semi-transparent to transparent and lack internal structure. It is bounded above by a hummocky reflector of high amplitude. Within the inlet, AF1 mostly occurs as an irregular to hyperbolic geometries underlying AF2. Its basal stratigraphic position beneath all other identified acoustic facies indicates that it predates the

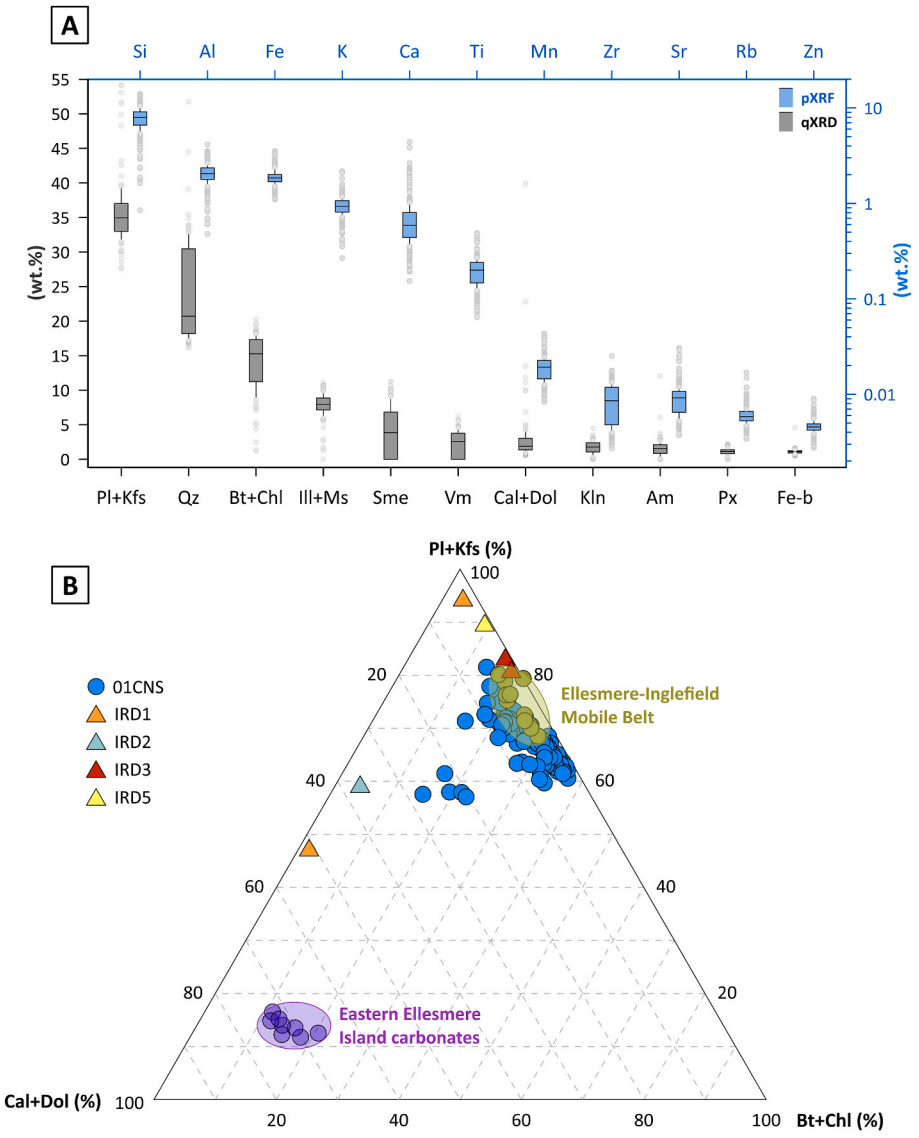

Fig. 6. **(A)** Boxplot of the chemical (pXRF) distributions of the main elements (wt.%; blue) and the mineralogical (qXRD) distributions of the main minerals (wt.%; gray) within the composite core. Note that the relative concentrations obtained with the pXRF sensor were converted to percentages (1% = 10,000 ppm) for better visualization. **(B)** Mineralogical ternary plot of plagioclase + K-feldspar (Pl+Kfs) – biotite + chlorite (Bt+Chl) – calcite + dolomite (Cal+Dol) for cores 01CNS (this study) and 01 PC (Stevenard et al., 2022). The source data for eastern Ellesmere Island carbonates (purple circles) are from Bicera-Nfundiko (2024), and those for the Ellesmere-Inglefield Mobile Belt (green circles) are from Stevenard et al. (2022). (For interpretation of the references to color in this figure legend, the reader is referred to the Web version of this article.)

overlying deposits, although no direct age constraints are available because AF1 was not recovered in the sediment cores. Based on its acoustic characteristics and stratigraphic position, the AF1 facies is interpreted as the acoustic basement, likely representing either glacial till or bedrock.

The **AF2** facies is acoustically semitransparent, with weak and chaotic internal reflections that tend to diminish with depth in some areas. This facies is characterized by a strong, mostly continuous upper reflector and a lower-amplitude basal reflector, which occasionally lacks a clear delineation with the underlying AF1. AF2 is overprinted by single- and multi-crested ridges of various sizes that lie directly on AF1 and are either covered by AF3 or exposed at the seafloor. These ridges show discontinuous and chaotic internal reflections and correspond to areas marked by moraines and crevasse-squeeze ridges identified on the swath bathymetric imagery. Based on its acoustic characteristics and correlations with moraines and crevasse-squeeze ridges, the AF2 facies is interpreted as till deposited during periods of glacial stillstand and/or readvances during deglaciation or episodic warming periods.

The **AF3** facies is massive and ranges from acoustically semi-transparent to stratified, with weak-amplitude internal reflectors. It is bounded by a strong, continuous upper reflector and a strong, mostly continuous basal reflector. AF3 occurs throughout the inlet and is generally exposed at the seafloor, infilling the spaces between the multi-crested AF2 ridges. It is also observed in a few basin-like areas beneath AF4 (Fig. 5A). The thickness of AF3 typically ranges from 3 to 4 m. The massive, semi-transparent to stratified acoustic character suggests a mixture of depositional processes reflecting variations in lithology or sediment density. Based on correlation with lithological data, we suggest two main depositional processes for AF3: (1) an ice-proximal supply of suspended sediment resulting in the deposition of laminated mud corresponding to LF1 (Fig. 7 and Table 4), and (2) suspension settling from ice-distal meltwater plumes resulting in the deposition of glaciomarine sediments corresponding to LF2 (Fig. 7 and Table 4). The transition between AF3 and AF4 is not recorded in the sediment core 01CS as there is no significant change in density (Fig. 7).

The **AF4** facies is acoustically stratified, characterized by weak-

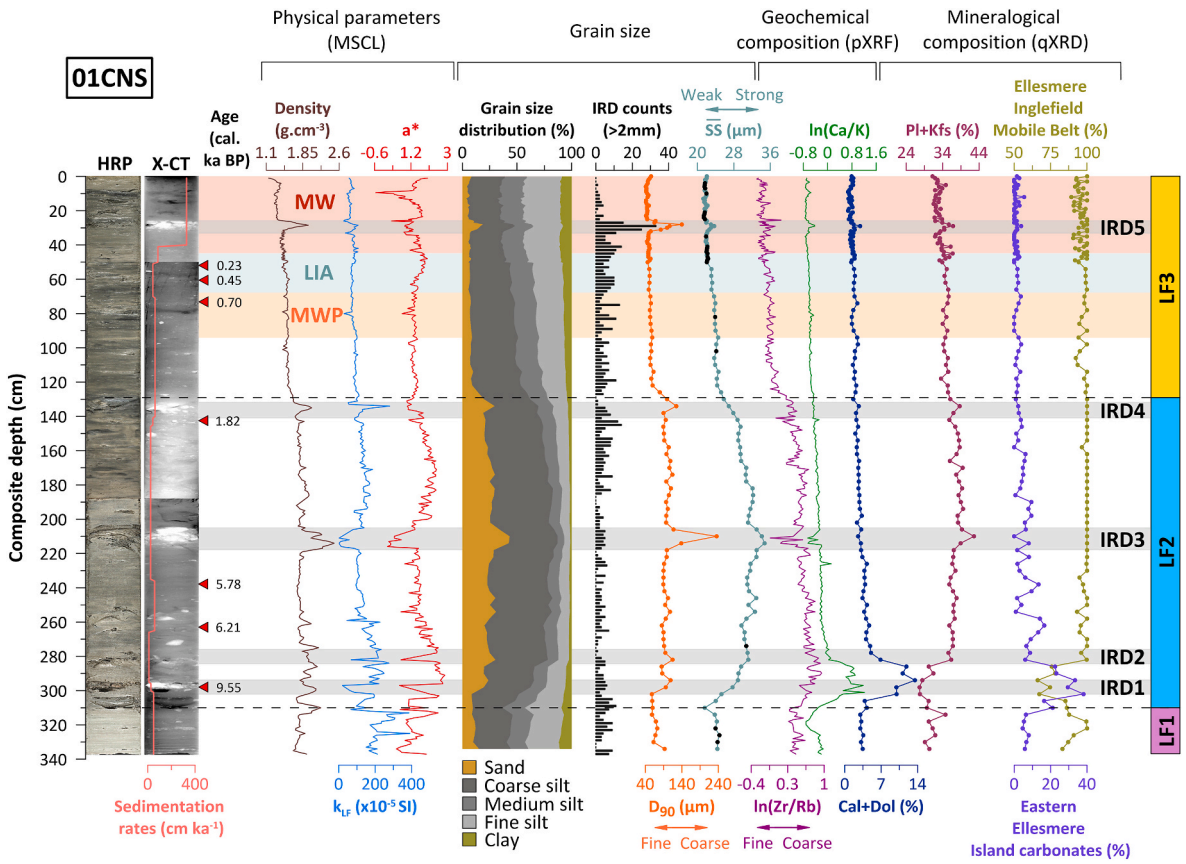

Fig. 7. High-resolution core photography, X-CT image, sedimentation rates, magnetic susceptibility (k_{LF}), a*, grain size distribution, IRD counts (>2 mm fraction), D_{90} (µm), mean size of sortable silt fraction ($\overline{SS}$), chemical and mineralogical tracers, SedUnMix results with the proportions of sediment from Eastern Ellesmere Island carbonates (purple) and Ellesmere-Inglefield Mobile Belt (green), and sedimentary units. The red triangles represent the radiocarbon dates. IRDs are numbered and highlighted in gray boxes. Black dots on the $\overline{SS}$ curve represent samples that do not pass the reliability test of a downcore correlation coefficient >0.5 between $\overline{SS}$ and SS%. MW: Medieval Warming, LIA: Little Ice Age, MW: Modern Warming. (For interpretation of the references to color in this figure legend, the reader is referred to the Web version of this article.)

amplitude internal reflectors. It ranges in thickness from 1.3 to 2.5 m and is bounded by a strong, continuous lower reflector and the seafloor. AF4 conformably overlies AF3, but only in basin-like areas. Similar to AF3, its stratification likely reflects variations in lithology or sediment density. Based on its correlation with lithological data, AF4 is interpreted as a late Holocene glaciomarine mud deposited by suspension settling from ice-distal meltwater plumes, corresponding to LF3 (Fig. 7 and Table 4).

The **AF5** facies is acoustically transparent to semi-transparent, with chaotic and poorly defined internal reflectors. It displays a distinctive lobe-shape geometry and appears interbedded with AF3. This facies is observed exclusively on the distal flank of the terminal moraine in the inner part of the inlet. Based on its geometry and correlation with bathymetric data, AF5 is interpreted as a debris-flow deposit, possibly a debris lobe.

4.3. Sediment cores

4.3.1. Elemental composition (pXRF) and mineralogical assemblage (qXRD)

The boxplot of major element compositions (pXRF) for the bulk sediment fraction of core 01CNS is dominated by Si (~0.85–14.1%), Al (~0.5–4.2%), Fe (~1.1–3.6%), K (~0.3–2.2%), Ca (~0.2–4.4%), and Ti (~0.06–0.5), with lower concentrations of Mn, Zr, Sr, Rb and Zn (<0.1%) (Fig. 6A).

The mineralogical assemblage (qXRD) of the <2 mm bulk sediment fraction, illustrated by both qXRD boxplots and a ternary plot (Pl + Kfs - Cal + Dol - Bt + Chl), indicates that core 01CNS is primarily composed (>90%) of Pl + Kfs (28–43%), Qz (16–35%), Bt + Chl (7–20%), Ill + Ms (6–11%), Sme (0–11%), Vm (0–6%), and Cal + Dol (0.6–14%), with minor proportions (<5%) of Kln, Am, Px, and Fe-b minerals (Fig. 6A). The mineralogical composition of the >2 mm fraction of four ice-rafted debris-rich layers (IRD1 to IRD3 and IRD5) was also analyzed and plotted on the ternary plot, except for IRD4 due to insufficient material (Fig. 6B). IRD1 is composed of a mix of Pl + Kfs and Cal + Dol, IRD2 is rich in Cal + Dol, and IRD3 and IRD5 are dominated by Pl + Kfs. Mineralogical variations throughout the core (Fig. 7) show that it is mainly composed of crystalline minerals, with average contents of 35% Pl + Kfs (up to 42.6% at 210 cm) and 15% Chl + Bt (up to 20.3% at 6 cm). However, the base of the core records a detrital carbonate-rich interval (282-306 cm), marked by a synchronous increase in the ln (Ca/K) ratio to 1.2 and a rise in Cal + Dol content to 13.5%. The mineralogical signatures of the IRDs (Fig. 6B) support this source shift observed at the base of the core. These results suggest that most of the sediment originates from the Ellesmere-Inglefield Mobile Belt, with a temporary shift to a more distal carbonate-rich source from eastern Ellesmere Island (Nares Strait) during the deposition of the basal interval (Fig. 7).

4.3.2. Sedimentary lithofacies

The sediment core record consists of three sedimentary lithofacies (LF; Fig. 7 and S5) determined based on visual core descriptions, high-resolution core photographic images (HRP), X-CT scan images, physical and chemical properties, grain size parameters, and mineralogical

Table 3
Summary of the five acoustic lithofacies identified in Cape Norton Shaw Inlet with their associated descriptions and interpretations.

Acoustic facies	Images	Description	Interpretations
AF5	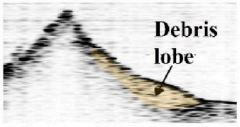	• semi-transparent to transparent • no internal structure • distinctive lobate geometry	Debris-flow deposits (Debris lobe)
AF4	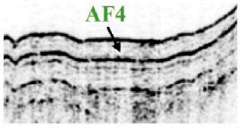	• stratified reflections • strong and continuous upper and lower reflectors	Glacimarine sediments
AF3	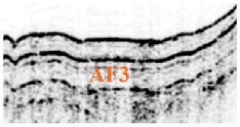	• stratified reflections • strong and continuous upper reflector • continuous to discontinuous lower reflector	Glacimarine sediments
AF2	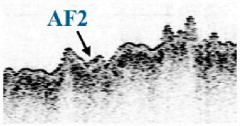	• semi-transparent • weak and chaotic internal reflections • overprinted by single- and multi-crested ridges • overlaying AF1	Glacimarine sediments reworked by pushing and squeezing processes (moraines, MSGLs and CSRs)
AF1	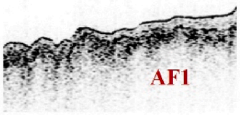	• semi-transparent to transparent • no internal structure • impenetrable and discontinuous upper surface reflector of high amplitude	Acoustic basement

Table 4
Summary of the physical characteristics, average grain size data (D_{90}) and interpretation of the depositional processes of the lithofacies identified in core 01CNS.

	X-CT	HRP	Lithofacies	Colour	Sedimentary structures	D_{90} (μm)	Depositional processes
LF3	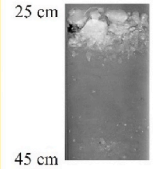	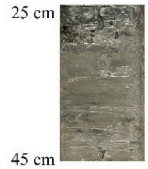	Silty mud with IRDs	2.5Y 4/2 Olive gray	• Massive mud • Dispersed IRDs • Single IRD layer	53	• Ice rafting • Meltwater plumes
LF2	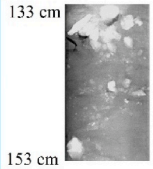	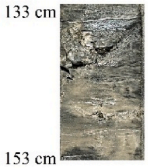	Sandy to silty mud with IRDs	2.5Y 4/2 Olive gray	• Dispersed IRDs • Four IRD layers with shell fragments	100	• Ice rafting • Turbidity events
LF1	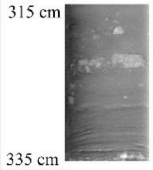		Silty laminated mud with IRDs	2.5Y 5/1 Gray	• Parallel laminations, few are oxidized • Dispersed IRDs	69	• Ice rafting • Meltwater plumes

assemblages of composite core 01CNS (Fig. 7). The results are summarized in Table 4.

LF1 (337-310 cm; 9.8-10.4 cal ka BP) is characterized by grayish silty sediments with millimeter- and centimeter-sized laminations associated with high k_{LF} values (226 SI x 10^{-5}; Fig. 7). Visible on the HRP, few laminations range from brown to red, indicating iron oxidation. Several centimeter-sized IRDs are interspersed in these laminations. The lithofacies displays no variation in terms of the grain size distribution, the geochemical or mineralogical compositions. The $\overline{SS}$ profile displays consistently low values (~24 μm), indicating stable near-bottom current

intensity (Fig. S6). LF1 is interpreted as proximal glaciogenic sediments deposited near the ice margin under calm conditions within a meltwater-dominated depositional environment. These sediments probably represent the early stage of the deglaciation phase of the inlet during the early Holocene. The transition from LF1 to LF2 is characterized by a noticeable change in sediment color, a decrease in k_{LF}, and an increase in the proportion of coarser sediments and near-bottom current intensity (Fig. 7 and S6).

LF2 (310-129 cm; 1.6-9.8 cal ka BP) is characterized by an olive-gray color. The sediments are predominantly coarse, consisting of ~24% sand and ~50% coarse silts, as indicated by the ln(Zr/Rb) and D_{90} profiles, as well as grain-size distribution data. $\overline{SS}$ values increase throughout the unit, reaching high values (up to ~30 μm), which suggest the presence of intensified near-bottom current activity during this interval (Fig. S6). Numerous centimeter-scale IRDs are scattered throughout LF2, with their abundance increasing toward the top of the unit. This lithofacies contains four distinct layers of coarser sediments interpreted as IRDs (Fig. S4), located at 294-302 cm (IRD1), 281-287 cm (IRD2), 205-218 cm (IRD3), and 132-141 cm (IRD4). These layers are characterized by increases in D_{90} and the sand content, along with decreases in k_{LF} and a* values (Fig. 7 and S4). Broken shell fragments are present in IRD1, IRD2 and IRD3. Overall, the lithofacies records low sedimentation rates with rather high wet bulk density (1.9 g cm^{-3}), k_{LF} (132 SI × 10^{-5}) and a* (1.8).

From 306 to 282 cm, the sediments, rich in Pl + Kfs (~31%), show a sudden increase in Cal + Dol (~9%) associated with the deposition of IRD1 and IRD2. Sediment provenance analysis indicates a mixture of proximal sources from the Ellesmere Inglefield Mobile Belt (~80%) and a more distal contribution from eastern Ellesmere Island carbonates (~20%). These results suggest a period of enhanced export of carbonate-rich IRDs associated with deglaciation and the opening of Nares Strait during the early Holocene (~9 cal ka BP; Jennings et al., 2011, 2019; Georgiadis et al., 2018). From 282 to 129 cm, the lithofacies is characterized by higher proportions of Pl + Kfs (~37%) and Chl + Bt (~12.5%), along with a return to lower Cal + Dol content (~3%). The sediment provenance during this interval is dominated by the Ellesmere Inglefield Mobile Belt (~99%). The lowermost part of LF2 is interpreted as a mixture of sediments: one component derived from surrounding landmasses and deposited distal to the ice margin of the glacier, and another from IRDs delivered by icebergs and sea ice coming from outside Cape Norton Shaw Inlet. The upper portion of the unit provides evidence that warmer conditions have led to an accelerated landward retreat of the Cape Norton Shaw Inlet glaciers. The transition from LF2 to LF3 is marked by a decrease in coarse sediments, wet bulk density, and k_{LF} and by an increase in the Chl + Bt content (Fig. 7).

LF3 (129–0 cm; 1.6 cal ka BP to present day) is characterized by olive-gray silty sediments. Compared to LF2, it exhibits lower values in physical parameters (wet bulk density, k_{LF}, a*), grain size (D_{90}) and elemental ratios ln(Zr/Rb) and ln(Ca/K), and Pl + Kfs content (Fig. 7). The generally decreasing $\overline{SS}$ values exhibit a short and rapid increase coinciding with the deposition of IRD5, suggesting that this layer was deposited during a short-lived event involving strong near-bottom currents and/or shift in provenance. Toward the top of the unit, the proportion of coarse and medium silt decreases from 60 to 50%, while clay content increases from 7 to 9%. Sand content remains relatively stable at ~7%. The highest concentration of IRDs (>2 mm) in the core is observed between 26 and 83 cm (Fig. 7 and S4), with an average of ~9 IRDs and a peak of 33 IRDs in IRD5 (26-33 cm). This peak indicates a marked increase in ice-rafted debris input during this interval, reflecting enhanced delivery of coarse-grained material to the site. IRD5 is further characterized by an increase in coarser, poorly sorted material in the <2 mm fraction (Fig. S4), along with elevated values of k_{LF}, ln(Ca/K), and higher percentages of Cal + Dol and Pl + Kfs. Sedimentation rates increase progressively throughout LF3, reaching their highest levels in the uppermost 40 cm. LF3 was probably deposited during a period of enhanced glacial meltwater outwash, driven by increasing atmospheric temperatures.

4.3.3. Chronology

The ^{210}Pb activity profile of core 33BC (Fig. S3) shows exponential decay, with a ^{210}Pb-supported value of ~24 Bq kg^{-1}. This value is consistent with those observed in the Smith Sound region ranging from ~20 to 30 Bq kg^{-1} (e.g., Bailey et al., 2013; Ribeiro et al., 2021; Bracquart et al., 2025; Koerner et al., 2025). Based on excess ^{210}Pb, the sediments in the upper 12 cm of the composite core present a typical remobilization curve (Arias-Ortiz et al., 2018); the data from this interval were thus not used to establish the chronology (Fig. S3). Therefore, 01CNS spans the last 10.4 cal ka BP, with a median calculated sedimentation rate of 50 cm ka^{-1} (Fig. 8). The model reveals seven

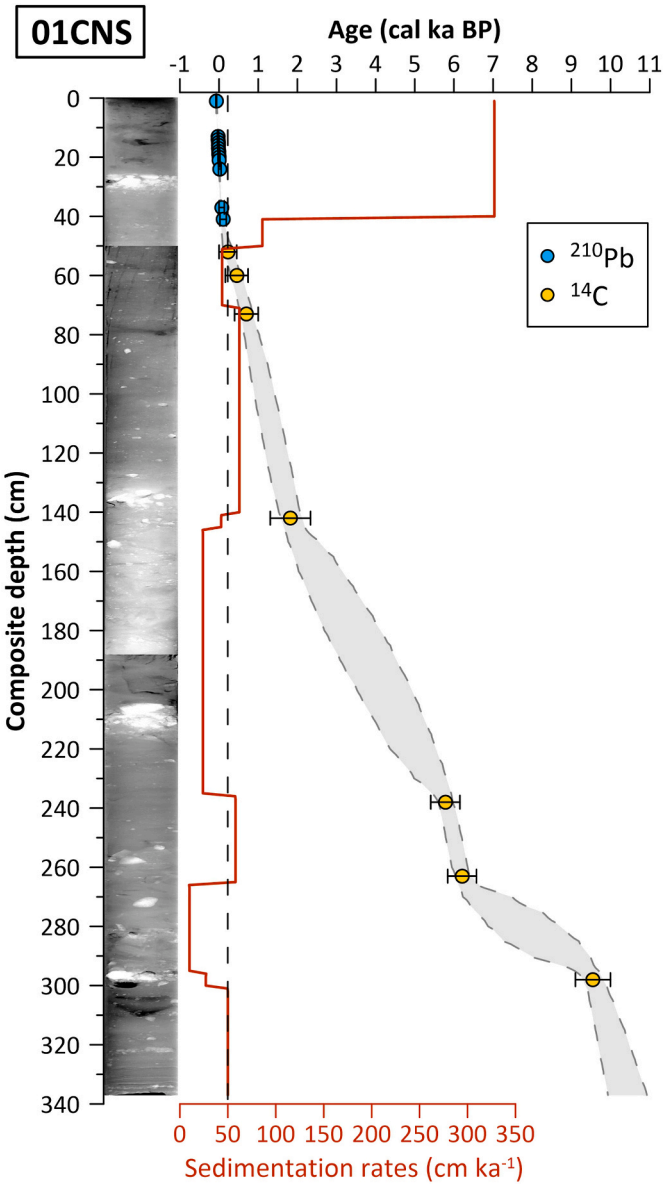

Fig. 8. Composite age-depth model for core 01CNS constructed using ^{210}Pb and ^{14}C ages. The Bayesian age–depth model was constructed using the R package rbacon (version 3.3.1; Blaauw and Christen, 2011). The gray shading represents the chronological uncertainties (95% confidence interval). The black dotted line represents the median of the data for the sedimentation rates. The estimated sedimentation rates in cm ka^{-1} are also shown. (For interpretation of the references to color in this figure legend, the reader is referred to the Web version of this article.)

major changes in sedimentation rates throughout the Holocene: 1) a high sedimentation rate of 50 cm ka^{-1} during the early Holocene (10.4-9.65 cal ka BP; 337–301 cm depth), 2) followed by a decrease to 10 cm ka^{-1} from the early to middle Holocene (9.65-6.3 cal ka BP; 300-266 cm depth), 3) a brief increase of 58 cm ka^{-1} during the middle Holocene (6.2–5.7 cal ka BP; 265-236 cm depth), 4) a long decrease to 24 cm ka^{-1} during the middle to late Holocene (5.7-1.9 cal ka BP; 235-146 cm depth), 5) an increase to 62 cm ka^{-1} 6) followed by a short decrease to 44 cm ka^{-1}during the late Holocene (1.9 cal ka BP to 1749 CE; 145-51 cm depth) and 7) a very high sedimentation rate to 328 cm ka^{-1} during the last ~270 years (50-0 cm).

5. Discussion

The combination of sediment cores, swath bathymetry imagery and acoustic sub-bottom profiles allowed identifying a sedimentological, mineralogical and geomorphological record typical of advances and retreats of glaciers (e.g., Dowdeswell et al., 2016; Stevenard et al., 2022). Here we discuss the evolution of the IIS and the glacier extents and dynamics across the inlet linked to climate and oceanic changes since the Younger Dryas which can explain the observed patterns (Fig. 9, Fig. 10, Fig. 11andFig. 12).

5.1. Transition from the IIS to the Manson Icefield (prior to 10.4-8.2 cal ka BP)

Swath bathymetry at the entrance of Cape Norton Shaw Inlet reveals at least four grounding-zone wedges followed by a cluster of moraines (Fig. 2A-B). This assemblage reflects a stepwise style of deglaciation, in which overall grounding-line retreat was modulated by episodic still-stands or minor re-advances. The formation of grounding-zone wedges implies sustained sediment delivery at the grounding line, likely supported by high subglacial sediment flux and a relatively stable ice margin, enabling their formation over decadal to centennial timescales (Dowdeswell et al., 2008; Dowdeswell and Fugelli, 2012; Batchelor and Dowdeswell, 2015). Grounding-zone wedges are commonly interpreted as evidence of Younger Dryas stillstands and readvances on Baffin Island and Greenland coasts (e.g., Young et al., 2012, 2020; Larsen et al., 2016; Funder et al., 2021). Although submarine Younger Dryas landforms have not yet been specifically documented in the fjords of Ellesmere Island, similar assemblages identified by Brouard and Lajeunesse (2019a) and Belko et al. (2026) along Baffin Bay suggest that the ice

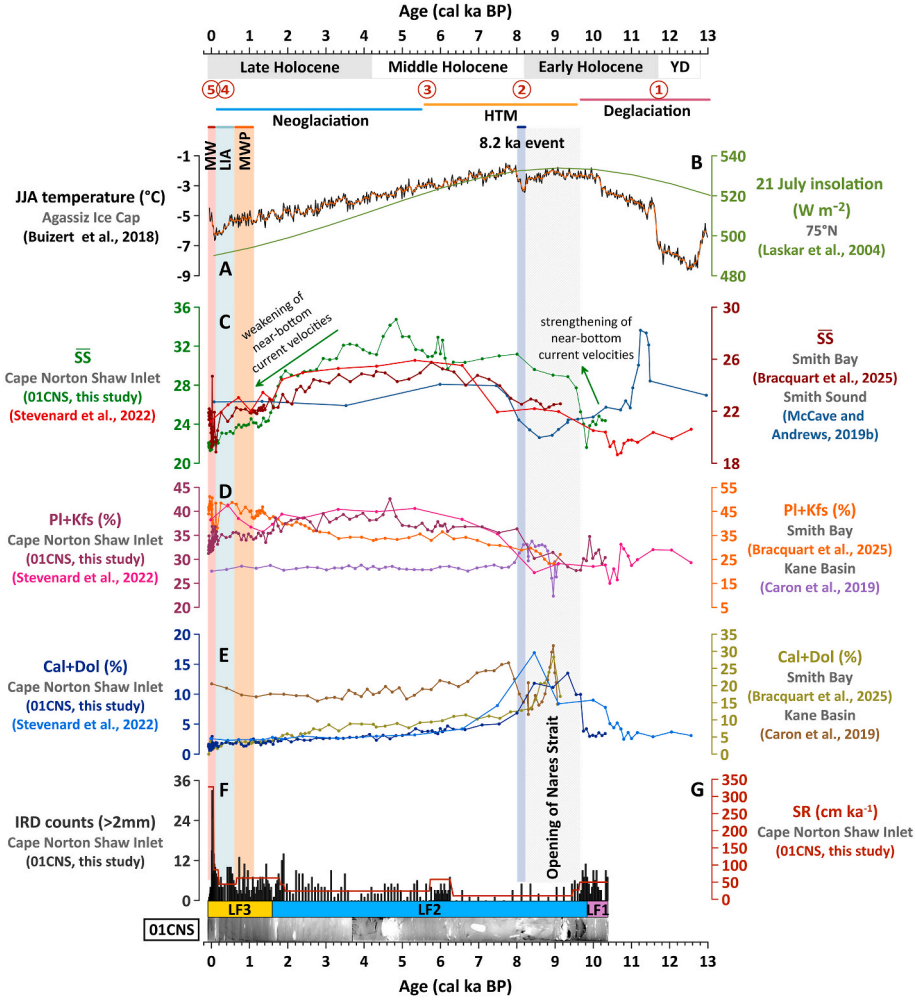

Fig. 9. Comparison of proxies used in this study (01CNS) with paleoenvironmental proxies. **(A)** Reconstructed summer temperature (°C) of the Agassiz Ice Cap (Buizert et al., 2018). **(B)** 21 July insolation at 75°N (Laskar et al., 2004). **(C)** Mean size of sortable silt fraction ($\overline{SS}$) from cores 01CNS (green, this study), 01MCS (dark red, Bracquart et al., 2025), AMD1803-01 PC (red, Stevenard et al., 2022) and 2001LSSL-014PC (blue, McCave and Andrews, 2019b), **(D)** Pl + Kfs (%) from cores 01CNS (crimson, this study), 01MCS (orange, Bracquart et al., 2025), AMD1803-01 PC (pink, Stevenard et al., 2022) and AMD14-Kane2B (purple, Caron et al., 2019), **(E)** Cal + Dol (%) from cores 01CNS (dark blue, this study), 01MCS (green, Bracquart et al., 2025), AMD1803-01 PC (light blue, Stevenard et al., 2022) and AMD14-Kane2B (gold, Caron et al., 2019), **(F)** IRD count (>2 mm), and **(G)** sedimentation rates (cm ka^{-1}) from cores 01CNS (this study). #1 to #5 indicates conditions shown in Fig. 10A–E. (For interpretation of the references to color in this figure legend, the reader is referred to the Web version of this article.)

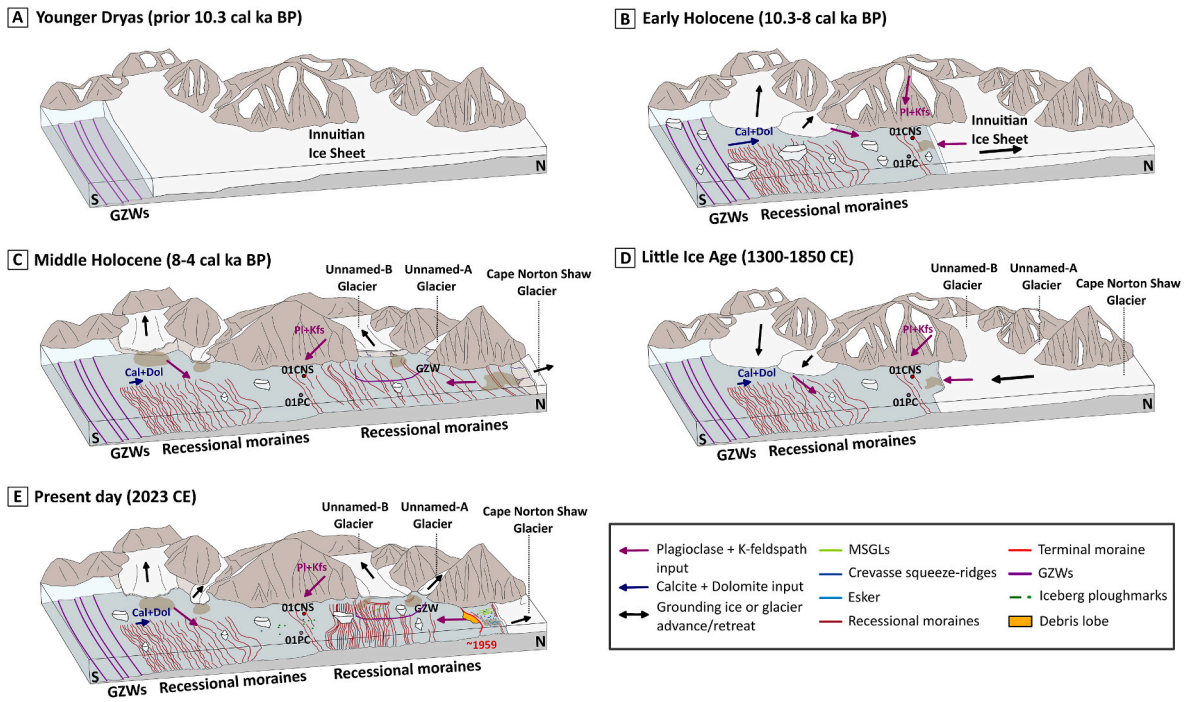

Fig. 10. Reconstruction of the sedimentary processes and environmental conditions in Cape Norton Shaw Inlet during the: **(A)** Younger Dryas (prior to 10.3 cal ka BP), **(B)** early Holocene (10.3-8 cal ka BP), **(C)** middle Holocene (8-4 cal ka BP), and late Holocene (4 cal ka BP to present), with a distinction between **(D)** the Little Ice Age (LIA; ~1300-1850 CE) and **(E)** the present day (2023 CE).

sheet margin stabilized near fjord mouths during this interval. In Cape Norton Shaw Inlet, in the absence of direct chronological constraints, the position of grounding-zone wedges at the inlet entrance leads us to infer that these grounding-zone wedges represent the maximum extent of the IIS during the Younger Dryas (Fig. 11A), although a more distal ice limit cannot be excluded.

The moraine cluster (25-28 ridges), located further inland and stratigraphically overlying the grounding-zone wedges, formed during subsequent stages of ice-margin retreat. The transition from grounding-zone wedges to a moraine cluster may indicate a shift in ice-margin dynamics, with reduced sediment delivery and/or increased sensitivity to external forcing, such as ocean-driven melt or changes in ice discharge, promoting more frequent oscillations of the grounding line (e.g., Dowdeswell et al., 2008). The relatively regular spacing and morphology of these ridges suggest that they may correspond to closely spaced retreat moraines, potentially analogous to De Geer moraine-type landforms formed during successive ice readvances (e.g., Dowdeswell et al., 2008; Benn and Evans, 2010). However, in the absence of direct dating, it is not possible to confidently assign an annual origin. The moraines are therefore interpreted as recording frequent, short-readvances of the retreating ice margin. Sub-bottom profiles show that the spaces between the moraines are infilled with sediments associated with the Holocene facies AF2-3 (Table 3 and Fig. 5), suggesting that the moraines predate the Holocene. Together, the grounding-zone wedge–moraine succession provides a near-continuous record of grounding-line behavior, capturing both decadal to centennial-scale stability (grounding-zone wedges) and higher-frequency retreat oscillations (moraines) from the Younger Dryas to the Early Holocene.

Following the Younger Dryas, the onset of the Holocene was marked by warmer conditions than today (Fig. 9A), leading to the final collapse of the IIS and LIS and their landward retreats in northeastern Baffin Bay (e.g., Marcott et al., 2013; Lecavalier et al., 2017; Buizert et al., 2018; Dalton et al., 2023). In Cape Norton Shaw Inlet, the base of core 01 PC studied by Stevenard et al. (2022) reveals a sequence of upward-thinning sandy laminations, ranging from centimeter to millimeter scale within Unit 1, closely resembling those observed in LF1 at the base of core 01CNS from this study (Fig. 7 and S5). These laminations were interpreted as hyperpycnal flow deposits and are thought to document the retreat of the ice margin during deglaciation. This succession of ice-proximal sediments suggests that: (1) the ice margin gradually retreated from the core site, (2) this retreat was relatively continuous, and (3) it was not interrupted by any major glacier readvance. Although the thinner laminations described by Stevenard et al. (2022) resemble those reported here, mineralogical correlations between the two sediment cores suggest that their proposed age model yields older dates than this study (Fig. S7). The discrepancy is likely due to the absence of a basal date in core 01 PC, which limits the accuracy of their age model. Therefore, the basal date from core 01CNS is preferred, as it provides the oldest documented age for the deglaciation and indicates that half of the inlet was already ice-free before 10.4 cal ka BP. The retreat sequence recorded in both cores is consistent with the presence of moraines near the core sites (Fig. 2).

Between 10.4 and 9.7 cal ka BP, relatively high sedimentation rates (~50 cm ka^{-1}), high k_{LF} values (~212 × 10^{-5} SI), high coarse silt content (up to 37%), the presence of laminations, and sparse IRDs at the base of LF1 suggest enhanced glacial activity and an increased supply of suspended sediment during this interval (Fig. 7). The Pl + Kfs-rich layer probably reflects the release of local material derived from the Ellesmere Inglefield Mobile Belt, associated with the retreat of the ice margin (Fig. 7 andFig. 9D). At the base of LF2, between 9.7 and 8.4 cal ka BP, elevated concentrations of detrital carbonates indicate that ~25% of the sediments originated from carbonate-rich sources on eastern Ellesmere Island (Figs. 7 and 9and Fig. 9E). Two distinct IRD-rich layers (IRD1 and IRD2) composed of unsorted material are observed in this unit (Fig. S4). Given the distance of core 01CNS from active glacier fronts at the time, these IRD-rich layers are likely associated with major ice breakup events and increased iceberg calving, reflecting episodes of climatic warming. At this stage, the formerly extensive ice margin may have retreated sufficiently to fragment into smaller, modern-style glacier systems (Fig. 10B). IRD1 and IRD2 suggest that the sedimentation near core 01CNS was mainly influenced by ice-rafted material from the calving fronts of Cape Norton Shaw Glacier, with minor contributions from

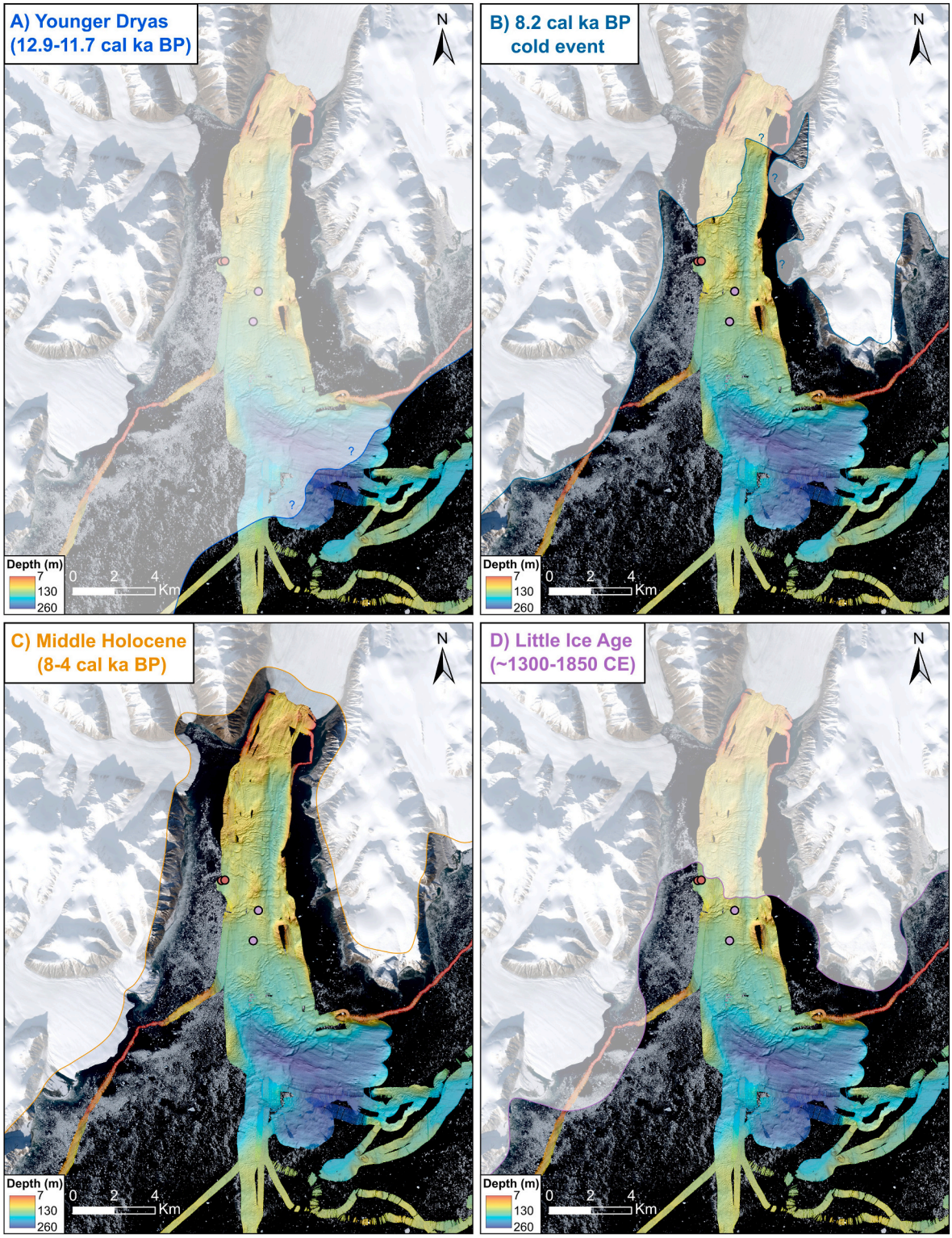

Fig. 11. Reconstruction of the ice extent over Cape Norton Shaw Inlet for the **(A)** Younger Dryas, **(B)** 8.2 cal ka BP cold event, **(C)** Middle Holocene (8-4 cal ka BP), and **(D)** Little Ice Age (~1300-1850 CE). Sentinel-2 image from 14 September 2023 (source: copernicus.eu) with swath bathymetric data from CCGS *Amundsen* and S/Y *Vagabond*. The ice-extent limits were modified from Dalton et al. (2023). (For interpretation of the references to color in this figure legend, the reader is referred to the Web version of this article.)

external sources. The increase in $\overline{SS}$ records from 10.4 to 8 cal ka BP indicates a long-term strengthening of near-bottom current velocities (Fig. 7, Fig. 9CFigs. 7 and 9 and S6). This trend suggests a shift in depositional energy driven by climatic-induced changes during the Early Holocene. At that time, warm temperatures triggered the retreat of the IIS, leading to enhanced meltwater discharge within Cape Norton Shaw Inlet as evidenced by relatively high sedimentation rates, high coarse content and laminations (Fig. 7). The increase in the $\overline{SS}$ records coincide with the deposition of two IRD-rich layers and elevated concentrations of detrital carbonates originating from the Nares Strait region,

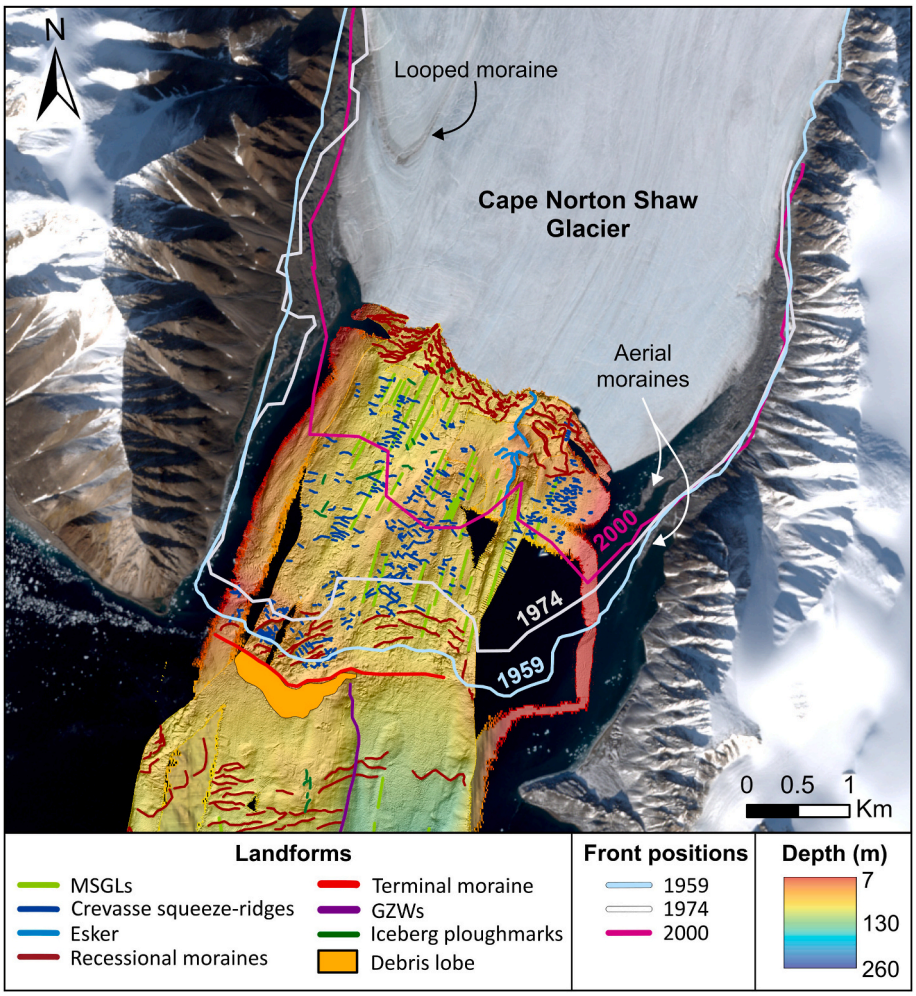

Fig. 12. Sentinel-2 image from 14 September 2023 (source: copernicus.eu) of the modern glacier front with swath bathymetric data from CCGS *Amundsen* and S/Y *Vagabond*. The colored lines represent the ice fronts in 1959 (light blue), 1974 (gray) and 2000 (pink). (For interpretation of the references to color in this figure legend, the reader is referred to the Web version of this article.)

suggesting that change in regional circulation patterns following the initial retreat of the IIS also had an impact on the strengthening of near-bottom current velocities within the inlet. According to ice reconstructions by Dalton et al. (2023), the Early Holocene sediments were likely deposited during the final opening of Jones Sound and deglaciation of Nares Strait (Jennings et al., 2011, 2019; Georgiadis et al., 2018; Caron et al., 2019, 2020; Stevenard et al., 2022).

The abrupt 8.2 cal ka BP cold event recorded in Greenland ice cores as a short-lived $\delta^{18}O$ anomaly linked to Laurentide meltwater freshwater discharge events into the northern North Atlantic is not recorded in core 01CNS (Fig. 7; Alley et al., 1997; Von Grafenstein et al., 1998; Barber et al., 1999). However, the large grounding-zone wedge identified on the swath bathymetry imagery in front of Unnamed B Glacier, which formed after the outer grounding-zone wedges and was partly overridden by younger moraines (Fig. 2B), likely marks the glacier front during this brief climatic perturbation, before retreating gradually (Fig. 11B). The timing remains uncertain but is broadly consistent with regional evidence for glacier expansion during this cold period (Solomina et al., 2015).

The absence of coalescence with an advance of Cape Norton Shaw Glacier indicates differing glacier responses. Both glaciers are tidewater, but available bathymetric data do not reveal clear contrasts in inlet geometry that could account for this difference. Alternative explanations remain therefore more speculative. One possibility is that Cape Norton Shaw Glacier had retreated further inland prior to the 8.2 cal ka BP cold event, resulting in different initial glacier configurations at the onset of cooling. Differences in catchment hypsometry may also have influenced glacier sensitivity. However, no quantitative data are currently available for either basin. As Manson Icefield is a known hotspot for surge-type glaciers (Copland et al., 2003), a surge-type origin for the grounding-zone wedge of Unnamed B Glacier cannot be entirely excluded. However, given the absence of comparable or more recent geomorphological evidence for repeated or cyclical surge activity in the landform record in front of Unnamed B Glacier, a surge-type origin for this grounding-zone wedge is considered unlikely. Therefore, the contrasting responses of the two glaciers most likely reflect differences in pre-event glacier extent and initial dynamic configuration prior to the onset of the 8.2 cal ka BP cooling.

5.2. *Land-terminating glaciers during the Middle Holocene (8-2 cal ka BP)*

The decrease in the detrital carbonate content (Fig. 7) observed in LF2 at the beginning of the middle Holocene suggests a reduced input of carbonate-rich sediments from Nares Strait and Jones Sound into the inlet due to reduced ice rafting transport. This period coincides with the full opening of marine connections between the Arctic Ocean and Baffin Bay (e.g., Jennings et al., 2011, 2019; Furze et al., 2018; Kelleher et al., 2022; Dalton et al., 2023; Okuma et al., 2023), facilitating broader oceanic circulation and sediment redistribution. This reduction in

detrital carbonates input aligns with the onset of the Holocene Thermal Maximum (HTM), a period of summer temperatures warmer than present conditions throughout the Arctic, driven by high boreal summer insolation around 8 cal ka BP (Fig. 9A–B; e.g., Kaufman et al., 2004; Mayewski et al., 2004; Marcott et al., 2013; Briner et al., 2016; Lecavalier et al., 2017; Buizert et al., 2018). Between ~8 and 4.7 cal ka BP, low sedimentation rates (Fig. 8) combined with an increase in coarse silt and sand content (Fig. 7) suggest a decline in fine-grained sediment delivery via sea ice, reflecting a landward retreat of surrounding glaciers (Fig. 10C). The enrichment in Pl+Kfs in coarse-grained sediments (Fig. 7) reflects an enhanced delivery of locally derived glacial material, possibly linked to enhanced erosion and sediment transport from surrounding landmasses during periods of glacier retreat. As suggested by Stevenard et al. (2022), terrestrial glaciers can deliver gravel-sized sediments across fan deltas. Given the proximity of the core site 01CNS to the coast, IRD3, composed of unsorted material and shell fragments (Fig. S4), may reflect such a depositional process. In this context, we infer that Cape Norton Shaw Inlet glaciers were either actively retreating or had transitioned to land-based systems in response to the mid-Holocene warming and the absence of the IIS (Figs. 10C and 11C). Such a retreat is consistent with the broader Arctic response to the Holocene Thermal Maximum, during which glaciers and ice-sheet margins commonly receded to extents smaller than today (e.g., Larsen et al., 2015; McKay et al., 2018). From ~4.7 to ~2 cal ka BP, a gradual decline in coarse sediment content suggests a progressive return to colder conditions (Fig. 7 and Fig. 9A) Figs. 7 and 9 that favored glacier regrowth to near-modern extents during the initial phase of the Neoglaciation.

5.3. Retreat of the glaciers during the late Holocene (2 cal ka BP to present)

From ~1.9 cal ka BP to ~1850 CE, the general increase in sediment rates, IRD content, and finer-grained sediments within LF3 (Figs. 7 and 9F-G) suggest an intensification of glacial erosion processes in Cape Norton Shaw Inlet. The decrease in $\overline{SS}$ records, and therefore the reduced near-bottom current velocity at that time, is consistent with the interpretation that the late Holocene in Smith Sound region was characterized by a gradual weakening of circulation associated with declining insolation and reduced meltwater input (Fig. 9A–C; McCave and Andrews, 2019b; Stevenard et al., 2022; Bracquart et al., 2025). As evidenced by the temperature reconstructions from Agassiz Ice Cap (Fig. 9A), the intensification of the glacial erosional processes is linked to the extensive regrowth of the tidewater glaciers in the inlet during the second phase of the Neoglaciation (Briner et al., 2009, 2016; Solomina et al., 2015; McKay et al., 2018; Buizert et al., 2018), which culminated during the Little Ice Age (~1300-1850 CE; Grove, 1988). Moreover, a sediment core collected ~40 km south-east of Cape Norton Shaw Inlet (Core AMD19-2.5BC) by Koerner et al. (2025), shows stable geochemical signals and consistently low total dinocyst fluxes between 1670 and 1920 CE, suggesting a prolonged seasonal sea ice cover. Similar findings, including high fluxes of the sea ice biomarker IP_{25}, have been reported in Nares Strait (Georgiadis et al., 2020), further supporting the presence of favorable conditions for glacier regrowth in the region during this period (Fig. 10D).

Swath bathymetry imagery reveals a prominent cluster of 30-40 morainic ridges aligned with the modern front of Cape Norton Shaw Glacier (Fig. 2), suggesting a direct association with this glacier system. This moraine cluster overlies both the Younger Dryas-Early Holocene moraine assemblage and the grounding-zone wedge attributed to the 8.2 cal ka BP event, confirming its relatively young age. A smaller cluster of moraines is also visible in front of Unnamed-B Glacier (Fig. 2). In northern Baffin Bay, the Little Ice Age was the only late-Holocene period with sufficiently cold conditions to drive extensive glacier readvances and consequently produce such a large number of retreat moraines (Fig. 9A; Briner et al., 2016). Therefore, we interpret this moraine cluster as marking the maximum Little Ice Age extent of Cape Norton Glacier and its subsequent retreat toward its present-day position punctuated by likely annual short-lived readvances. The moraine distribution suggests that during the Little Ice Age the glacier advanced nearly to the middle of the inlet, approaching its Early Holocene extent (Figs. 10D and 11D), highlighting the sensitivity of the glacier to relatively brief climatic perturbations.

Since approximately 1900 CE, the onset of a markedly warmer period associated with glacier retreat is evidenced by high sedimentation rate (368 cm ka^{-1}) in the upper 40 cm of core 01CNS (Fig. 9G). A similar trend is observed in Smith Bay, where sedimentation rates range from 163 to 223 cm ka^{-1} (Bracquart et al., 2025), attributed to increased runoff from snowmelt and meltwater plumes. In southern Nares Strait, sedimentation rates of ~400-700 cm ka^{-1} have been recorded, reflecting shorter ice-arch durations or their failure in Kane Basin (Jackson et al., 2021; Ribeiro et al., 2021). IRD5 is enriched in both Pl + Kfs and Cal + Dol, indicating a mixed provenance (Fig. 7 and S4). Given the distance of the coring sites from active glacier fronts and their proximity to inlet cliffs (Fig. 1A), the presence of gravel-sized sediments rich in Pl + Kfs is most probably related to increased runoff from snowmelt and/or rockslides from the cliffs. Satellite imagery shows that icebergs from Nares Strait enter the inlet (Fig. S8A–C), potentially transporting gravel-sized sediments rich in Cal + Dol to the coring sites. Concurrently, the generally decreasing $\overline{SS}$ record exhibits an abrupt increase (Fig. 7), suggesting an intensification of near-bottom currents during a period of enhanced snowmelt inputs.

Overall, the observed glacial retreat is largely attributed to rising temperatures (Fig. 9A; Buizert et al., 2018), driven by the rapid and intense emission of anthropogenic greenhouse gases and aerosols since the onset of the Industrial Period (~1900 CE; Kaufman et al., 2009), despite a continued decrease in boreal summer insolation (Fig. 9B; Laskar et al., 2004; Kaufman et al., 2009). In the Arctic, warming is occurring up to four times faster than in the global average, leading to a significant reduction in the duration and extent of sea-ice cover (Kwok, 2018). Tidewater glaciers, which are common throughout the CAA and particularly in Cape Norton Shaw Inlet, are especially vulnerable to climate change due to their exposure to both atmospheric and oceanic forcings (Noël et al., 2018; Cook et al., 2019). Based on the spacing (~30m) of the ten moraines closest to the modern ice front (Fig. 12), a minimum retreat rate of ~30 m yr^{-1} is inferred for the decade 2013-2023. This estimate assumes that the moraines formed annually and does not account for potential gaps in the record or variability in the timing of moraine formation.

5.4. Historical surge of Cape Norton Shaw Glacier

Approximately 4 km from the present-day front of Cape Norton Shaw Glacier (Fig. 12), the seafloor is covered by numerous submarine landforms formed under varying glaciological conditions. These landforms reflect different phases of ice flows and glacier dynamics. Given their proximity to the modern frontal position of Cape Norton Shaw Glacier and the absence of overprinting by younger landforms, this assemblage likely marks the recent glacier activity.

Along the NNE–SSW axis of the inlet, elongated ridges interpreted as mega-scale glacial lineations record a phase of fast glacier flow. mega-scale glacial lineations are bounded by two clusters of relatively evenly spaced De Geer moraines, indicating slower retreat periods before and after this episode, and are locally crosscut by shorter, rhombohedral crevasse-squeeze ridges, reflecting subsequent stagnation and slow retreat under a heavily crevassed ice margin. Together, these landforms are truncated by a prominent transverse ridge interpreted as a terminal moraine, marking a maximum glacier extent, while a sinuous ridge extending from the glacier front, interpreted as an esker, indicates a subglacial meltwater channel that remains active today, as suggested

by the presence of a tunnel and associated sediment plume observed during the 2019 Vagabond and 2023 Amundsen expeditions (Fig. 4B). This assemblage of mega-scale glacial lineations, crevasse-squeeze ridges, eskers, terminal and retreat moraines have been widely documented in association with surge-type glaciers, particularly in regions such as Svalbard and Iceland. They are considered diagnostic indicators of surge activity (e.g., Evans and Rea, 2003; Streuff et al., 2015; Dowdeswell and Ottesen, 2016; Ingólfsson et al., 2016; Ottesen et al., 2017; Flink and Noormets, 2018; Osika and Jania, 2024).

Cape Norton Shaw Glacier was described as surge-type by Copland et al. (2003). The identification was based on the observation of distinct surge landforms such as a looped moraine on the west side of the glacier and the presence of numerous crevasses at its terminus on aerial photographs from the summer of 1959 CE (Fig. S1), as well as a retreat of ~2 km between 1959 and 1999 CE (Copland et al., 2003). Collectively the submarine landforms mapped in this study confirm the surge-type behavior of Cape Norton Shaw Glacier. The complete surge cycle can be reconstructed, beginning with a phase of rapid glacier advance forming mega-scale glacial lineations during the active phase of the surge, which lasted until ~1959 CE. The rapid glacier advance was followed by maximum extent marked by the terminal moraine at the end of the surge ~1959 CE, and subsequent stagnation and slow retreat recorded by crevasse-squeeze ridges and retreat moraines during the current quiescent phase. Although precise dates for the beginning and the end of the surge cannot be determined due to the lack of aerial photographs before 1959 CE, and the absence of satellite images between 1959 and 1974 CE, the position of the terminal moraine on the bathymetric image is ~250 m beyond the glacier front observed in the summer of 1959 (Fig. 12), indicating that the glacier was still advancing or had recently started retreating at that time. Between the terminal moraine and the 1974 ice front position (Fig. 12), when the first LANDSAT images became available, three retreat moraines were identified. Assuming an annual retreat, we estimate that at least three years of retreat occurred prior to 1974, which implies that the glacier entered its active phase before 1959 and reached its maximum extent between the summers of 1959 and 1971 CE. The active surge phase therefore lasted at least 15 years, a duration comparable to, although slightly shorter than, the ~20-year cycle reported for other surge-type glaciers in the CAA (e.g., Copland et al., 2003, 2024; Millan et al., 2017; Van Wychen et al., 2020, 2022; Lauzon et al., 2023). The 1959 ice front also corresponds to a lateral aerial moraine on the east side of the glacier (Fig. 12). Dating both the terminal and lateral moraines would provide a more precise age for the end of the active phase. No evidence of a previous surge is visible in the bathymetric images, nor is there any indication of a more recent surge in satellite images. The glacier is today in its quiescent phase, with an estimated retreat of ~44 m yr^{-1} between 1974 and 2023 CE.

Bracquart et al. (2025) proposed that the 1992-2007 surge of Mittie Glacier may have been associated by increased precipitation in 1991 CE. However, Cape Norton Shaw Glacier did not experience a surge around 2000, as shown by satellite images and the absence of characteristic post-1959 submarine landforms. Similarly, Mittie Glacier does not appear to have surged ~1959 CE, based on aerial photographs. These observations indicate that, despite their geographic proximity, the timing of the surge initiation differs between the two glaciers. This asynchrony suggests that surge initiation is primarily controlled by internal glacier dynamics, while external climatic factors may modulate glacier mass balance and influence long-term system preconditioning, rather than directly triggering surge events. We acknowledge that disentangling internal variability from potential indirect climatic influences remains challenging given the available temporal constraints.

6. Conclusions

In this paper, we provide a detailed reconstruction of sedimentary dynamics and ice margin positions in Cape Norton Shaw Inlet since the Younger Dryas based on an approach combining sediment cores with swath bathymetry imagery and sub-bottom acoustic stratigraphy. These results lead to the following key conclusions:

- The swarm of 30-40 large recessional moraines overlying the grounding-zone wedges at the inlet entrance indicates a retreat of the ice margin following the Younger Dryas cold event.
- Between 10.4 and 9.7 cal ka BP, millimeter-to centimeter-scale laminations lacking grain-size grading, along with the presence of IRDs in LF1, indicate a depositional environment dominated by meltwater outwash and suspensions settling in a distal ice-proximal setting within Cape Norton Shaw Inlet.
- The combined evidence of increased detrital carbonate content in both mineralogical and geochemical records, low sedimentation rates (~20 cm ka^{-1}), and enhanced near-bottom current velocity support the hypothesis of a gradual opening of Nares Strait between 9.6 and 8 cal ka BP.
- The low sedimentation rates (<30 cm ka^{-1}) recorded in LF2 between 8 and 1.7 cal ka BP, along with the coarse-grained sediments enriched in Pl and Kfs, indicate local sediment discharge associated with the landward retreat of glaciers bordering the inlet.
- The presence of recessional moraines across the inlet supports a gradual retreat of the ice margin from the Younger Dryas through to the Neoglacial period.
- During the Neoglacial period, the increase in IRD content and finer-grained sediments in LF3, combined with the presence of a large swarm of recessional moraines, suggests a readvance of Cape Norton Shaw Glacier into the inlet, reaching its Holocene maximum extent.
- The near-glacial submarine landform assemblage, including mega-scale glacial lineations, crevasse-squeeze ridges, eskers, terminal and retreat moraines, represents a complete surge-cycle signature and confirm the surge-type behavior of Cape Norton Shaw Glacier.
- The close correspondence between the terminal moraine position and the 1959 glacier front confirms that a surge initiated around 1959 CE, with the glacier reaching its maximum extent between 1959 and 1971 CE.
- The landforms imprinted on the seafloor of Cape Norton Shaw Inlet outline processes associated with subglacial (mega-scale glacial lineations, crevasse-squeeze ridges, eskers), ice-marginal (grounding-zone wedges, terminal moraine ridges, recessional moraine ridges), and glaciomarine (iceberg ploughmarks) environments.
- Based on the position of the grounding-zone wedges and the swarms of recessional moraines across the inlet, the ice extent positions for the Younger Dryas and the Holocene periods previously proposed have been updated.

By building on previous paleoclimate and paleoenvironmental reconstructions in the inlet, these results provide new insights into the past dynamics of surrounding glaciers and refine the retreat history of the IIS in the Cape Norton Shaw Inlet, including glacier extent reconstructions.

Author contributions

Conceptualization: EB, JCMS, PL, LC; Formal Analysis: EB, JCMS, PL; Funding acquisition: JCMS, PL, LC, GSO, AH; Investigation: EB, JCMS, AH, GJ; Methodology: EB, JCMS, PL, GSO; Resources: JCMS, PL, LC, GSO, AH; Supervision: JCMS, PL, LC, GSO; Visualization: EB, GJ; Writing-original draft: EB; Writing-review and editing; EB, JCMS, PL, LC, GSO, AH, GJ.

Declaration of competing interest

The authors declare the following financial interests/personal relationships which may be considered as potential competing interests:

Andrew Hamilton and Gabriel Joyal report Sonic 2026 multibeam echosounder was provided by R2Sonic. If there are other authors, they

declare that they have no known competing financial interests or personal relationships that could have appeared to influence the work reported in this paper.

Acknowledgments

Some of the data presented herein were collected by the Canadian research icebreaker CCGS *Amundsen* and made available by the Amundsen Science program, in accordance with the Data Policy and Management (2025). We are grateful to the captain, officers, crew and scientists onboard the CCGS Amundsen during the 2017, 2018 and 2023 ArcticNet expeditions and onboard the S/Y Vagabond during the summer 2019 expedition for the acquisition of swath bathymetry data and the recovery of the sediment cores used in this study. We thank Quentin Beauvais (ISMER-UQAR) for his help with X-CT scans, physical property and geochemical analyses; Claude Belzile (ISMER-UQAR) for his advice with the grain size analyses; and Daniel Amirault (Amundsen Science) and Kerstin Brembach (U. Laval and Amundsen Science) for the bathymetry dataset processing.

This research was supported by ArcticNet (funded by the Strategic Science Fund), Amundsen Science, and the Geotop (https://doi.org/10.69777/341269; https://doi.org/10.69777/377326) and Québec-Océan (https://doi.org/10.69777/309012) research clusters, both funded by the Fonds de recherche du Québec. Additional support was provided by the Natural Sciences and Engineering Research Council of Canada (NSERC) through Discovery Grants and Northern Supplements awarded to JCMS, PL, GSO, and LC , as well as a Research Tools and Instruments grant awarded to PL. Additional financial support for the 2019 *Vagabond* cruise was provided by the Canadian Hydrographic Service to GJ and AH. R2Sonic contributed in-kind support by providing a Sonic 2026 multibeam echosounder for the 2019 *Vagabond* cruise. JG also received support from the Centre de géomatique du Québec. EB was funded through an ISMER excellence scholarship and a PBEEE-FRQNT scholarship (No. 350396; https://doi.org/10.69777/350396). Finally, we thank two anonymous reviewers for their constructive reviews, which significantly improved the quality of the manuscript. We also thank Bethan Davies for her editorial support.

Appendix A. Supplementary data

Supplementary data to this article can be found online at https://doi.org/10.1016/j.quascirev.2026.110139.

Data availability

All analytical data presented will be available electronically in the PANGAEA database (https://www.pangaea.de/).

References

Alley, R.B., Mayewski, P.A., Sowers, T., Stuiver, M., Taylor, K.C., Clark, P.U., 1997. Holocene climatic instability: a prominent, widespread event 8200 yr ago. Geology 25 (6), 483–486.

Amundsen Science Data Collection, 2017a. Bathymetric data collected by the CCGS Amundsen in the Canadian Atlantic/Arctic. Processed data. Limited distribution. Accessed from amundsen.data@as.ulaval.ca, on 06/09/2024.

Amundsen Science Data Collection, 2018a. Bathymetric data collected by the CCGS Amundsen in the Canadian Atlantic/Arctic. Processed data. Limited distribution. Accessed from amundsen.data@as.ulaval.ca, on 06/09/2024.

Amundsen Science Data Collection, 2023a. Bathymetric data collected by the CCGS Amundsen in the Canadian Atlantic/Arctic. Processed data. Limited distribution. Accessed from amundsen.data@as.ulaval.ca, on 06/09/2024.

Amundsen Science Data Collection, 2017b. Acoustic sub-bottom profiles (3.5 khz) collected onboard the CCGS Amundsen – acoustic mapping of the seabed relief and shallow subsurface sediments. https://doi.org/10.5884/12942. www.polardata.ca. CCIN:12942. (Accessed 5 May 2025).

Amundsen Science Data Collection, 2018b. Acoustic sub-bottom profiles (3.5 khz) collected onboard the CCGS Amundsen – acoustic mapping of the seabed relief and shallow subsurface sediments. https://doi.org/10.5884/12942. www.polardata.ca. CCIN:12942. (Accessed 5 May 2025).

Amundsen Science Data Collection, 2023b. Acoustic sub-bottom profiles (3.5 khz) collected onboard the CCGS Amundsen – acoustic mapping of the seabed relief and shallow subsurface sediments. Limited distribution. Accessed from amundsen.data@as.ulaval.ca, on 06/09/2024.

Andrews, J.T., 2000. Icebergs and iceberg rafted detritus (IRD) in the North Atlantic: facts and assumptions. Oceanography (Wash. D. C.) 13 (3), 100–108. https://doi.org/10.5670/oceanog.2000.19.

Andrews, J.T., Bjork, A.A., Eberl, D.D., Jennings, A.E., Verplanck, E.P., 2015. Significant differences in late Quaternary bedrock erosion and transport: east versus West Greenland ~70° N–evidence from the mineralogy of offshore glacial marine sediments. J. Quat. Sci. 30, 452–463. https://doi.org/10.1002/jqs.2787.

Andrews, J.T., Stein, R., Moros, M., Perner, K., 2016. Late Quaternary changes in sediment composition on the NE Greenland margin (~ 73° N) with a focus on the fjords and shelf. Boreas 45, 381–397. https://doi.org/10.1111/bor.12169.

Andrews, J.T., Eberl, D.D., 2012. Determination of sediment provenance by unmixing the mineralogy of source-area sediments: the "SedUnMix" program. Mar. Geol. 291, 24–33. https://doi.org/10.1016/j.margeo.2011.10.007.

Arias-Ortiz, A., Masqué, P., Garcia-Orellana, J., Serrano, O., Mazarrasa, I., Marbà, N., Lovelock, C.E., Lavery, P.S., Duarte, C.M., 2018. Reviews and syntheses: 210 Pb-derived sediment and carbon accumulation rates in vegetated coastal ecosystems–setting the record straight. Biogeosciences 15 (22), 6791–6818. https://doi.org/10.5194/bg-15-6791-2018.

Bailey, J.N.L., Macdonald, R.W., Sanei, H., Outridge, P.M., Johannessen, S.C., Hochheim, K., Barber, D., Stern, G.A., 2013. Change at the margin of the North Water Polynya, Baffin Bay, inferred from organic matter records in dated sediment cores. Mar. Geol. 341, 1–13. https://doi.org/10.1016/j.margeo.2013.04.017.

Banerjee, I., McDonald, B.C., 1975. Nature of Esker Sedimentation.

Barber, D.C., Dyke, A., Hillaire-Marcel, C., Jennings, A.E., Andrews, J.T., Kerwin, M.W., Bilodeau, G., McNeely, R., Southon, J., Morehead, M.D., Gagnon, J.M., 1999. Forcing of the cold event of 8,200 years ago by catastrophic drainage of Laurentide Lakes. Nature 400 (6742), 344–348.

Batchelor, C.L., Krawczyk, D.W., O'Brien, E., Mulder, J., 2024. Shelf-break glaciation and an extensive ice shelf beyond northwest Greenland at the last Glacial Maximum. Mar. Geol. 476, 107375. https://doi.org/10.1016/j.margeo.2024.107375.

Batchelor, C.L., Dowdeswell, J.A., 2015. Ice-sheet grounding-zone wedges (GZWs) on high-latitude continental margins. Mar. Geol. 363, 65–92. https://doi.org/10.1016/j.margeo.2015.02.001.

Belko, A.P., Lajeunesse, P., Normandeau, A., Couette, P.-O., Brouard, E., 2025. The role of inland ice dynamics in controlling the variable maximum extent of the Laurentide Ice Sheet off southeastern Baffin Island. Boreas 54, 468–479. https://doi.org/10.1111/bor.70000.

Belko, A.P., Normandeau, A., Lajeunesse, P., Limoges, A., 2026. Early deglaciation history of the southeastern Baffin Island shelf (Eastern Canadian Arctic Archipelago). J. Quat. Sci. 1–16. https://doi.org/10.1002/jqs.70067.

Belzile, C., Montero-Serrano, J.-C., 2022. Quantifying simulated fine sand fraction in muddy sediment using laser diffraction. Can. J. Earth Sci. 59 (7), 455–461. https://doi.org/10.1139/cjes-2022-0011.

Benn, D., Evans, D., 2010. Glaciers and glaciation. In: Hodder Education, second ed.

Ben-Yehoshua, D., Aradóttir, N., Farnsworth, W.R., Benediktsson, Í.Ö., Ingólfsson, Ó., 2023. Formation of crevasse-squeeze ridges at Trygghamna, Svalbard. Earth Surf. Process. Landf. 48 (12), 2334–2348. https://doi.org/10.1002/esp.5631.

Bjarnadóttir, L.R., Ottesen, D., Dowdeswell, J.A., Bugge, T., 2016. Unusual iceberg ploughmarks on the Norwegian continental shelf. In: Dowdeswell, J.A., Canals, M., Jakobsson, M., Todd, B.J., Dowdeswell, E.K., Hogan, K.A. (Eds.), Atlas of Submarine Glacial Landforms: Modern, Quaternary and Ancient, vol. 46. Geological Society, London, Memoir, pp. 283–284.

Blaauw, M., Christen, J.A., 2011. Flexible paleoclimate age–depth models using an autoregressive gamma process. Bayesian Analysis 6, 457–474. https://doi.org/10.1214/11-BA618.

Blake Jr., W., 1975. Radiocarbon age determinations and postglacial emergence at Cape Storm, southern Ellesmere Island, Arctic Canada. Geogr. Ann. Phys. Geogr. 1–71.

Blake Jr., W., 1993. Holocene emergence along the Ellesmere Island coasts of northernmost Baffin Bay. Nor. Geol. Tidsskr. 73 (3), 147–160.

Blott, S.J., Pye, K., 2001. GRADISTAT: a grain size distribution and statistics package for the analysis of unconsolidated sediments. Earth Surf. Process. Landf. 26, 1237–1248. https://doi.org/10.1002/esp.261.

Boulton, G.S., 1986. Push-moraines and glacier-contact fans in marine and terrestrial environments. Sedimentology 33 (5), 677–698.

Bracquart, E., Montero-Serrano, J.-C., Lajeunesse, P., St-Onge, G., Copland, L., 2025. The Holocene sedimentary record of Mittie Glacier dynamics in Smith Bay, Ellesmere Island (eastern Canadian Arctic Archipelago). J. Quat. Sci. 40, 1191–1211. https://doi.org/10.1002/jqs.70005.

Brennand, T.A., 2000. Deglacial meltwater drainage and glaciodynamics: inferences from Laurentide eskers, Canada. Geomorphology 32 (3–4), 263–293. https://doi.org/10.1016/S0169-555X(99)00100-2.

Briner, J.P., Davis, P.T., Miller, G.H., 2009. Latest Pleistocene and Holocene glaciation of Baffin Island, arctic Canada: key patterns and chronologies. Quat. Sci. Rev. 28, 2075e2087. https://doi.org/10.1016/j.quascirev.2008.09.017.

Briner, J.P., McKay, N.P., Axford, Y., Bennike, O., Bradley, R.S., de Vernal, A., Fisher, D., Francus, P., Fréchette, B., Gajewski, K., Jennings, A., Kaufman, D.S., Miller, G., Rouston, C., Wagner, B., 2016. Holocene climate change in Arctic Canada and Greenland. Quat. Sci. Rev. 147, 340–364. https://doi.org/10.1016/j.quascirev.2016.02.010.

Brouard, E., Lajeunesse, P., 2019a. Glacial to postglacial submarine landform assemblages in fiords of northeastern Baffin Island. Geomorphology 330, 40–56. https://doi.org/10.1016/j.geomorph.2019.01.007.

Brouard, E., Lajeunesse, P., 2019b. Submarine geomorphology of the northeastern Baffin Island fiords and cross-shelf troughs. J. Maps 15 (2), 662–676. https://doi.org/10.1080/17445647.2019.1647302.
Brown, R.J.E., 1972. Permafrost in the Canadian arctic Archipelago. Zeitschrift fur Geomorphologie 13, 102–130.
Bruel, R., Sabatier, P., 2020. Serac: an R package for ShortlivEd RAdionuclide chronology of recent sediment cores. J. Environ. Radioact. 225, 106449. https://doi.org/10.1016/j.jenvrad.2020.106449.
Buizert, C., Keisling, B.A., Box, J.E., He, F., Carlson, A.E., Sinclair, G., DeConto, R.M., 2018. Greenland-wide seasonal temperatures during the last deglaciation. Geophys. Res. Lett. 45 (4), 1905–1914. https://doi.org/10.1002/2017GL075601.
Butler, B., Hillier, S., 2021. powdR: an R package for quantitative mineralogy using full pattern summation of X-ray powder diffraction data. Comput. Geosci. 147, 104662. https://doi.org/10.1016/j.cageo.2020.104662.
Caron, M., Montero-Serrano, J.C., St-Onge, G., Rochon, A., 2020. Quantifying provenance and transport pathways of Holocene sediments from the northwestern Greenland margin. Paleoceanogr. Paleoclimatol. 34. https://doi.org/10.1029/2019PA003809.
Caron, M., Rochon, A., Montero-Serrano, J.C., St-Onge, G., 2019. Evolution of sea-surface conditions on the northwestern Greenland margin during the Holocene. J. Quat. Sci. 34, 569e580. https://doi.org/10.1002/jqs.3146.
Carr, J.R., Stokes, C.R., Vieli, A., 2013. Recent progress in understanding marine-terminating Arctic outlet glacier response to climatic and oceanic forcing: twenty years of rapid change. Prog. Phys. Geogr. 37 (4), 436–467. https://doi.org/10.1177/0309133313483163.
Chassiot, L., Lajeunesse, P., Francus, P., Normandeau, A., Lapointe, F., Massa, C., De Coninck, A., 2024. Landscape evolution and sediment delivery in a High Arctic proglacial Lake, Ellesmere Island, Canadian Arctic Archipelago. Earth Surf. Process. Landf. 49 (6), 1987–2009. https://doi.org/10.1002/esp.5811.
Ciracì, E., Velicogna, I., Swenson, S., 2020. Continuity of the mass loss of the world's glaciers and ice caps from the GRACE and GRACE follow-on missions. Geophys. Res. Lett. 47 (9). https://doi.org/10.1029/2019GL086926 e2019GL086926.
Clark, C.D., 1993. Mega-scale glacial lineations and cross-cutting ice flow landforms. Earth Surf. Process. Landf. 18, 1–29.
Cohen, J., Screen, J.A., Furtado, J.C., Barlow, M., Whittleston, D., Coumou, D., Francis, J., Dethloff, K., Entekhabi, D., Overland, J., Jones, J., 2014. Recent Arctic amplification and extreme mid-latitude weather. Nat. Geosci. 7 (9), 627–637. https://doi.org/10.1038/ngeo2234.
Cook, A.J., Copland, L., Noël, B.P.Y., Stokes, C.R., Bentley, M.J., Sharp, M.J., Bingham, R. G., van den Broeke, M.R., 2019. Atmospheric forcing of rapid marine-terminating glacier retreat in the Canadian Arctic Archipelago. Sci. Adv. 5. https://doi.org/10.1126/sciadv.aau8507 eaau8507.
Copland, L., Halle, D., Van Wychen, W., Lauzon, B., Dowdeswell, J.A., Davis, J., 2024. Characteristics of the 15-year surge of Mittie Glacier, SE Ellesmere Island, Canadian Arctic. Ann. Glaciol. 1–13. https://doi.org/10.1017/aog.2024.31.
Copland, L., Sharp, M.J., Dowdeswell, J.A., 2003. The distribution and flow characteristics of surge-type glaciers in the Canadian High Arctic. Ann. Glaciol. 36, 73–81. https://doi.org/10.3189/172756403781816301.
Couette, P.O., Lajeunesse, P., Ghienne, J.F., Dorschel, B., Gebhardt, C., Hebbeln, D., Brouard, E., 2022. Evidence for an extensive ice shelf in northern Baffin Bay during the last Glacial Maximum. Commun. Earth Environ. 3, 225. https://doi.org/10.1038/s43247-022-00559-7.
Couette, P.O., Lajeunesse, P., Ghienne, J.F., Dorschel, B., Gebhardt, C., Hebbeln, D., Brouard, E., 2023. Retreat and stabilization of a marine-based ice margin along a high arctic fjord-cross-shelf trough system. Quat. Sci. Rev. 302, 107949. https://doi.org/10.1016/j.quascirev.2022.107949.
Courtney, R., 2007. Storage and dissemination of SEGY data in JPEG2000 format. In: AGU Fall Meeting Abstracts, 2007. IN51B-0402.
Dalton, A.S., Dulfer, H.E., Margold, M., Heyman, J., Clague, J.J., Froese, D.G., Gauthier, M.S., Hughes, A.L.C., Jennings, C.E., Norris, S.L., Stoker, B.J., 2023. Deglaciation of the north American ice sheet complex in calendar years based on a comprehensive database of chronological data: NADI-1. Quat. Sci. Rev. 321, 108345. https://doi.org/10.1016/j.quascirev.2023.108345.
Dalton, A.S., Margold, M., Dulfer, H.E., Norris, S.L., Tarasov, L., 2024. Response of North American ice sheets to the Younger Dryas cold reversal (12.9 to 11.7 ka). Earth Sci. Rev. 255, 104845. https://doi.org/10.1016/j.earscirev.2024.104845.
De Geer, G.F., 1889. Ändmoräner i trakten mellan Spånga och Sundbyberg. GFF (Geol. Foren. Stockh. Forh.) 11, 395–397.
Dowdeswell, J.A., Canals, M., Jakobsson, M., Todd, B.J., Dowdeswell, E.K., Hogan, K.A., 2016. The variety and distribution of submarine glacial landforms and implications for ice-sheet reconstruction. Geological Society 46 (1), 519–552. https://doi.org/10.1144/m46.183. London, Memoirs.
Dowdeswell, J.A., Hamilton, G.S., Hagen, J.O., 1991. The duration of the active phase on surge-type glaciers: contrasts between Svalbard and other regions. J. Glaciol. 37 (127), 388–400. https://doi.org/10.3189/S0022143000005827.
Dowdeswell, J.A., Jakobsson, M., Hogan, K.A., O'Regan, M., Antony, D., Backman, J., Darby, D., Eriksson, B., Evans, D.J.A., Hell, B., Janzen, T., Löwemark, L., Marcussen, C., Noormets, R., Cofaigh, C.Ó., Polyak, L., Sellén, E., Sölvsten, M., 2010. High-resolution geophysical observations of the Yermak Plateau and northern Svalbard margin: implications for ice-sheet grounding and deep-keeled icebergs. Quat. Sci. Rev. 29 (25–26), 3518–3531. https://doi.org/10.1016/j.quascirev.2010.06.002.
Dowdeswell, J.A., Ottesen, D., Evans, J., Cofaigh, C.Ó., Anderson, J.B., 2008. Submarine glacial landforms and rates of ice-stream collapse. Geology 36 (10), 819–822. https://doi.org/10.1130/G24808A.1.
Dowdeswell, J.A., Fugelli, E.M.G., 2012. The seismic architecture and geometry of grounding-zone wedges formed at the marine margins of past ice sheets. Geol. Soc. Am. Bull. 124, 1750–1761. https://doi.org/10.1130/B30628.1.
Dowdeswell, J.A., Ottesen, D., 2013. Buried iceberg ploughmarks in the early Quaternary sediments of the central North Sea: a two-million year record of glacial influence from 3D seismic data. Mar. Geol. 344, 1–9. https://doi.org/10.1016/j.margeo.2013.06.019.
Dowdeswell, J.A., Ottesen, D., 2016. Eskers formed at the beds of modern surge-type tidewater glaciers in Spitsbergen. Geological Society, London, Memoirs 46 (1), 83–84. https://doi.org/10.1144/M46.70.
Dowdeswell, J.A., Ottesen, D., 2024. Iceberg ploughmarks and glacial lineations on Jan Mayen Ridge: evidence for past iceberg and possible ice-shelf grounding in deep water. Quat. Sci. Rev. 338, 108838. https://doi.org/10.1016/j.quascirev.2024.108838.
Dyke, A.S., Andrews, J.T., Clark, P.U., England, J.H., Miller, G.H., Shaw, J., Veillette, J. J., 2002. The laurentide and innuitian ice sheets during the last glacial maximum. Quat. Sci. Rev. 21 (1–3), 9–31. https://doi.org/10.1016/S0277-3791(01)00095-6.
Eberl, D.D., 2003. User's guide to RockJock – A program for determining quantitative mineralogy from powder X-ray diffraction data. U.S. Geological Survey Open-File Report 2003–78, 47p. https://doi.org/10.3133/ofr200378.
Evans, D.J.A., Storrar, R.D., Rea, B.R., 2016. Crevasse-squeeze ridge corridors: diagnostic features of late-stage palaeo-ice stream activity. Geomorphology 258, 40–50. https://doi.org/10.1016/j.geomorph.2016.01.017.
Evans, D.J.A., Rea, B.R., 1999. Geomorphology and sedimentology of surging glaciers: a land-systems approach. Ann. Glaciol. 28, 75–82. https://doi.org/10.3189/172756499781821823.
Evans, D.J.A., Rea, B.R., 2003. Surging glacier landsystem. In: Evans, D.J.A. (Ed.), Glacial Landsystems. Arnold, London, pp. 259–288.
Flink, A.E., Noormets, R., 2018. Submarine glacial landforms and sedimentary environments in Vaigattbogen, northeastern Spitsbergen. Mar. Geol. 402, 244–263. https://doi.org/10.1016/j.margeo.2017.07.019.
Funder, S., Goosse, H., Jepsen, H., Kaas, E., Kjær, K.H., Korsgaard, N.J., Larsen, N.K., Linderson, H., Lyså, A., Möller, P., Olsen, J., Willerslev, E., 2011. A 10,000-Year record of Arctic Ocean sea-ice variability—view from the beach. Science 333, 747–750. https://doi.org/10.1126/science.1202760.
Funder, S., Sørensen, A.H.L., Larsen, N.K., Bjørk, A.A., Briner, J.P., Olsen, J., Schomacker, A., Levy, L.B., Kjær, K.H., 2021. Younger Dryas ice margin retreat in Greenland: new evidence from southwestern Greenland. Clim. Past 17, 587–601. https://doi.org/10.5194/cp-17-587-2021.
Furze, M., Pienkowski, A., McNeely, M., Bennett, R., Cage, A., 2018. Deglaciation and ice shelf development at the northeast margin of the Laurentide Ice Sheet during the Younger Dryas chronozone. Boreas 47, 271–296. https://doi.org/10.1111/bor.12265.
Gales, J.A., Larter, R.D., Leat, P.T., 2016. Iceberg ploughmarks and associated sediment ridges on the southern Weddell Sea margin. In: Dowdeswell, J.A., Canals, M., Jakobsson, M., Todd, B.J., Dowdeswell, E.K., Hogan, K.A. (Eds.), Atlas of Submarine Glacial Landforms: Modern, Quaternary and Ancient, vol. 46. Geological Society, London, Memoir, pp. 289–290.
Georgiadis, E., Giraudeau, J., Jennings, A., Limoges, A., Jackson, R., Ribeiro, S., Massé, G., 2020. Local and regional controls on Holocene sea ice dynamics and oceanography in Nares Strait, Northwest Greenland. Mar. Geol. 422, 106115. https://doi.org/10.1016/j.margeo.2020.106115.
Georgiadis, E., Giraudeau, J., Martinez, P., Lajeunesse, P., St-Onge, G., Schmidt, S., Massé, G., 2018. Deglacial to postglacial history of Nares Strait, Northwest Greenland: a marine perspective from Kane Basin. Clim. Past 14, 1991–2010. https://doi.org/10.5194/cp-14-1991-2018.
Geyman, E.C., J. J. van Pelt, W., Maloof, A.C., et al., 2022. Historical glacier change on Svalbard predicts doubling of mass loss by 2100. Nature 601, 374–379. https://doi.org/10.1038/s41586-021-04314-4.
Grobe, H., 1987. A simple method for the determination of ice-rafted debris in sediment cores. Polarforschung 57, 123–126.
Grove, J.M., 1988. The Little Ice Age. Methuen, London.
Hamilton, A.K., Joyal, G., Copland, L., Myers, P.G., Brossier, E., 2021. Multibeam Sonar Data Collected from the 2019 SY Vagabond Cruise. Canadian Cryospheric Information Network (CCIN), Waterloo, Canada. Processed data. Version 1. Archived at. www.polardata.ca. https://www.polardata.ca/pdcsearch/PDCSearch.jsp?doi_id=13203.
Harrison, J.C., Thorsteinsson, R., Frisch, T., Mayr, U., Gilbert, C., Lynds, T., Ford, A., 2015. Geology, Tectonic Assemblage Map of Grise Fiord, Eastern Devon and Southern Ellesmere Islands, Nunavut, second ed., vol. 34. Geological Survey of Canada, Canadian Geoscience Map. https://doi.org/10.4095/296222. *preliminary), scale 1:500 000.*
Heaton, T.J., Köhler, P., Butzin, M., Bard, E., Reimer, R.W., Austin, W.E.N., Bronk Ramsey, C., Grootes, P.M., Hughen, K.A., Kromer, B., Reimer, P.J., Adkins, J., Burke, A., Cook, M.S., Olsen, J., Skinner, L.C., 2020. Marine20—The marine radiocarbon age calibration curve (0–55,000 cal BP). Radiocarbon 62 (4), 779–820. https://doi.org/10.1017/RDC.2020.68.
Huang, J., Zhang, X., Zhang, Q., Lin, Y., Hao, M., Luo, Y., Zhao, Z., Yao, Y., Chen, X., Wang, L., Nie, S., Yin, Y., Xu, Y., Zhang, J., 2017. Recently amplified arctic warming has contributed to a continual global warming trend. Nat. Clim. Change 7 (12), 875–879. https://doi.org/10.1038/s41558-017-0009-5.
Ingólfsson, Ó., Benediktsson, Í.Ö., Schomacker, A., Kjær, K.H., Brynjólfsson, S., Jonsson, S.A., Korsgaard, N.J., Johnson, M.D., 2016. Glacial geological studies of surge-type glaciers in Iceland—research status and future challenges. Earth Sci. Rev. 152, 37–69. https://doi.org/10.1016/j.earscirev.2015.11.008.

IPCC, 2023. IPCC, 2023: Climate Change 2023: Synthesis Report. Contribution of Working Groups I, II and III to the Sixth Assessment Report of the Intergovernmental Panel on Climate Change [Core Writing Team, H. Lee and J. Romero (eds.)]. In: Lee, H., Romero, J. (Eds.). IPCC, Geneva, Switzerland, p. 184. https://doi.org/10.59327/IPCC/AR6-9789291691647.

Jackson, R., Kvorning, A.B., Limoges, A., Georgiadis, E., Olsen, S.M., Tallberg, P., Andersen, T.J., Mikkelsen, N., Giraudeau, J., Massé, G., Wacker, L., Ribeiro, S., 2021. Holocene polynya dynamics and their interaction with oceanic heat transport in northernmost Baffin Bay. Sci. Rep. 11, 10095. https://doi.org/10.1038/s41598-021-88517-9.

Jakobsson, M., Mayer, L.A., Bringensparr, C., et al., 2020. The international bathymetric chart of the Arctic Ocean version 4.0. Sci. Data 7, 176. https://doi.org/10.1038/s41597-020-0520-9.

Jakobsson, M., O'Regan, M., 2016. Deep iceberg ploughmarks in the central Arctic Ocean. In: Dowdeswell, J.A., Canals, M., Jakobsson, M., Todd, B.J., Dowdeswell, E. K., Hogan, K.A. (Eds.), Atlas of Submarine Glacial Landforms: Modern, Quaternary and Ancient, vol. 46. Geological Society, London, Memoir, pp. 287–288.

Jennings, A.E., Andrews, J.T., Oliver, B., Walczak, M., Mix, A., 2019. Retreat of the smith sound ice stream in the early Holocene. Boreas 48, 825–840. https://doi.org/10.1111/bor.12391.

Jennings, A.E., Reilly, B., Andrews, J., Hogan, K., Walczak, M., Jakobsson, M., Stoner, J., Mix, A., Nicholls, K.W., O'Regan, M., Prins, M.A., Troelstra, S.R., 2022. Modern and early Holocene ice shelf sediment facies from Petermann Fjord and northern Nares Strait, northwest Greenland. Quat. Sci. Rev. 283. https://doi.org/10.1016/j.quascirev.2022.107460.

Jennings, A.E., Sheldon, C., Cronin, T., Francus, P., Stoner, J., Andrews, J., 2011. The Holocene history of Nares Strait: transition from glacial bay to Arctic–Atlantic throughflow. Oceanography (Wash. D. C.) 24, 26–41. https://doi.org/10.5670/oceanog.2011.52.

Kaufman, D.S., Ager, T.A., Anderson, N.J., et al., 2004. Holocene thermal maximum in the western Arctic (0–180°W). Quat. Sci. Rev. 23 (5–6), 529–560. https://doi.org/10.1016/j.quascirev.2003.09.007.

Kaufman, D.S., Schneider, D.P., McKay, N.P., Ammann, C.M., Bradley, R.S., Briffa, K.R., Miller, G.H., Otto-Bliesner, B.L., Overpeck, J.T., Vinther, B.M., Arctic Lakes 2k Project Members, 2009. Recent warming reverses long-term Arctic cooling. Science 325, 1236–1239. https://doi.org/10.1126/science.1173983.

Kelleher, R., Jennings, A., Andrews, J., Brooks, N.K., Marchitto, T., Feng, S., Woelders, L., Normandeau, A., Jenner, K., Bennett, R., Brookins, S., 2022. Late glacial retreat of the Lancaster Sound Ice Stream and early Holocene onset of Arctic/Atlantic throughflow in the Arctic Island channels. Arctic Antarct. Alpine Res. 54 (1), 395–427. https://doi.org/10.1080/15230430.2022.2110689.

Knudsen, K.L., Stabell, B., Seidenkrantz, M.-S., Eiríksson, J., Blake, W., 2008. Deglacial and Holocene conditions in northernmost Baffin Bay: sediments, foraminifera, diatoms and stable isotopes. Boreas 37, 346e376. https://doi.org/10.1111/j.1502-3885.2008.00035.x.

Kochtitzky, W., Copland, L., 2022. Retreat of Northern Hemisphere marine-terminating glaciers, 2000–2020. Geophys. Res. Lett. 49 (3). https://doi.org/10.1029/2021GL096501 e2021GL096501.

Koerner, K.A., Limoges, A., Pike-Connolly, E., Van Nieuwenhove, N., Rochon, A., 2025. Early impacts of Arctic amplification in the western North Water Polynya: a 400-year perspective. Mar. Micropaleontol., 102470 https://doi.org/10.1016/j.marmicro.2025.102470.

Kurjanski, B., Rea, B.R., Spagnolo, M., Winsborrow, M., Cornwell, D.G., Andreassen, K., Howell, J., 2019. Morphological evidence for marine ice stream shutdown, central Barents Sea. Mar. Geol. 414, 64–76. https://doi.org/10.1016/j.margeo.2019.05.001.

Kwok, R., 2018. Arctic sea ice thickness, volume, and multiyear ice coverage: losses and coupled variability (1958–2018). Environ. Res. Lett. 13, 105005. https://doi.org/10.1088/1748-9326/aae3ec.

Lajeunesse, P., 2016. Long continuous dendritic eskers offshore of Southampton Island, northern Hudson Bay. Geological Society 46, 87–88. https://doi.org/10.1144/M46.92. London, Memoirs.

Lajeunesse, P., Dietrich, P., Ghienne, J.F., 2019. Late wisconsinan grounding zones of the Laurentide ice sheet margin off the Québec north shore (NW Gulf of St lawrence). Geological Society, London, Special Publications 475 (1), 241–259. https://doi.org/10.1144/sp475.10.

Larsen, N.K., Funder, S., Linge, H., Möller, P., Schomacker, A., Fabel, D., Xu, S., Kjær, K. H., 2016. A Younger Dryas re-advance of local glaciers in north Greenland. Quat. Sci. Rev. 147, 47–58. https://doi.org/10.1016/j.quascirev.2015.10.036.

Larsen, N.K., Kjær, K.H., Lecavalier, B., Bjørk, A.A., Colding, S., Huybrechts, P., Jakobsen, K.E., Kjeldsen, K.K., Knudsen, K.L., Odgaard, B.V., Olsen, J., 2015. The response of the southern Greenland ice sheet to the Holocene thermal maximum. Geology 43 (4), 291–294. https://doi.org/10.1130/G36476.1.

Laskar, J., Robutel, P., Joutel, F., Gastineau, M., Correia, A.C.M., Levrard, B., 2004. A long-term numerical solution for the insolation quantities of the Earth. Astron. Astrophys. 428. https://doi.org/10.1051/0004-6361:20041335, 261e285.

Lauzon, B., Copland, L., Van Wychen, W., Kochtitzky, W., McNabb, R., Dahl-Jensen, D., 2023. Dynamics throughout a complete surge of Iceberg Glacier on western Axel Heiberg Island, Canadian High Arctic. J. Glaciol. 69 (277), 1333–1350. https://doi.org/10.1017/jog.2023.20.

Lecavalier, B.S., Fisher, D.A., Milne, G.A., Vinther, B.M., Tarasov, L., Huybrechts, P., Lacelle, D., Main, B., Zheng, J., Bourgeois, J., Dyke, A.S., 2017. High Arctic Holocene temperature record from the Agassiz ice cap and Greenland ice sheet evolution. Proc. Natl. Acad. Sci. USA 114, 5952–5957. https://doi.org/10.1073/pnas.1616287114.

Marcott, S.A., Shakun, J.D., Clark, P.U., Mix, A.C., 2013. A reconstruction of regional and global temperature for the past 11,300 years. Science 339 (6124), 1198–1201. https://doi.org/10.5194/wcd-6-43-2025.

Margreth, A., Gosse, J.C., Dyke, A.S., 2017. Wisconsinan and early Holocene glacial dynamics of Cumberland Peninsula, Baffin Island, Arctic Canada. Quat. Sci. Rev. 168, 79–100. https://doi.org/10.1016/j.quascirev.2017.04.033.

Mayewski, P.A., Rohling, E.E., Stager, J.C., Karlen, W., Maasch, K.A., Meeker, L.D., Meyerson, E.A., Gasse, F., van Kreveld, S., Holmgren, K., Lee-Thorp, J., Rosqvist, G., Rack, F., Staubwasser, M., Schneider, R.R., Steig, E.J., 2004. Holocene climate variability. Quaternary Research 62 (3), 243–255. https://doi.org/10.1016/j.yqres.2004.07.001.

McCave, I.N., Andrews, J.T., 2019a. Distinguishing current effects in sediments delivered to the ocean by ice. I. Principles, methods and examples. Quat. Sci. Rev. 212, 92–107. https://doi.org/10.1016/j.quascirev.2019.03.031.

McCave, I.N., Andrews, J.T., 2019b. Distinguishing current effects in sediments delivered to the ocean by ice. II. Glacial to Holocene changes in high latitude North Atlantic upper ocean flows. Quat. Sci. Rev. 223, 105902. https://doi.org/10.1016/j.quascirev.2019.105902.

McKay, N.P., Kaufman, D.S., Routson, C.C., Erb, M.P., Zander, P.D., 2018. The onset and rate of Holocene Neoglacial cooling in the Arctic. Geophys. Res. Lett. 45, 12487–12496. https://doi.org/10.1029/2018GL079773.

Meier, M.F., Post, A., 1969. What are glacier surges? Can. J. Earth Sci. 6 (4), 807–817. https://doi.org/10.1139/e69-081.

Millan, R., Mouginot, J., Rignot, E., 2017. Mass budget of the glaciers and ice caps of the Queen Elizabeth Islands, Canada, from 1991 to 2015. Environ. Res. Lett. 12 (2), 024016. https://doi.org/10.1088/1748-9326/aa5b04.

Montelli, A., Dowdeswell, J.A., Ottesen, D., Johansen, S.E., 2018. 3D seismic evidence of buried iceberg ploughmarks from the mid-norwegian continental margin reveals largely persistent North Atlantic Current through the Quaternary. Mar. Geol. 399, 66–83. https://doi.org/10.1016/j.margeo.2017.11.016.

Mundy, C.J., Gosselin, M., Ehn, J., Gratton, Y., Rossnagel, A., Barber, D.G., Martin, J., Tremblay, J.-E., Palmer, M., Arrigo, K.R., Darnis, G., Fortier, L., Else, B., Papakyriakou, T., 2009. Contribution of under-ice primary production to an ice-edge upwelling phytoplankton bloom in the Canadian Beaufort Sea. Geophys. Res. Lett. 36 (17). https://doi.org/10.1029/2009GL038837.

Noël, B., van de Berg, W.J., Lhermitte, S., Wouters, B., Schaffer, N., van den Broeke, M. R., 2018. Six decades of glacial mass loss in the Canadian Arctic Archipelago. J. Geophys. Res. Earth Surf. 123, 1430–1449. https://doi.org/10.1029/2017JF004304.

O'Regan, M., Cronin, T.M., Reilly, B., Alstrup, A.K.O., Gemery, L., Golub, A., Mayer, L.A., Morlighem, M., Moros, M., Munk, O.L., Nilsson, J., Pearce, C., Detlef, H., Stranne, C., Vermassen, F., West, G., Jakobsson, M., 2021. The Holocene dynamics of Ryder Glacier and ice tongue in north Greenland. Cryosphere 15 (8), 4073–4097. https://doi.org/10.5194/tc-15-4073-2021.

Okuma, E., Hingst, J., Weiser, J., Madaj, L., Titschack, J., Vogt, C., Kienast, M., Hillaire-Marcel, C., Hebbeln, D., Kasemann, S.A., 2023. Deglacial and Holocene sediment dynamics and provenances off Lancaster Sound: implications for paleoenvironmental conditions in northern Baffin Bay. Quat. Sci. Rev. 309, 108101. https://doi.org/10.1016/j.quascirev.2023.108101.

Omotoso, O., McCarty, D.K., Hillier, S., Kleeberg, R., 2006. Some successful approaches to quantitative mineral analysis as revealed by the 3rd Reynolds Cup contest. Clays Clay Miner. 54 (6), 748–760. https://doi.org/10.1346/CCMN.2006.0540609.

Osika, A., Jania, J., 2024. Geomorphological and historical records of the surge-type behaviour of Hansbreen (Svalbard). Ann. Glaciol. 65 (e31), 1–18. https://doi.org/10.1017/aog.2024.32.

Ottesen, D., Dowdeswell, J.A., Bellec, V.K., Bjarnadóttir, L.R., 2017. The geomorphic imprint of glacier surges into open-marine waters: examples from eastern Svalbard. Mar. Geol. 392, 1–29. https://doi.org/10.1016/j.margeo.2017.08.007.

Ottesen, D., Dowdeswell, J.A., Benn, D.I., Kristensen, L., Christiansen, H.H., Christensen, O., Hansen, L., Lebesbye, E., Forwick, M., Vorren, T.O., 2008. Submarine landforms characteristic of glacier surges in two Spitsbergen fjords. Quat. Sci. Rev. 27 (15–16), 1583–1599. https://doi.org/10.1016/j.quascirev.2008.05.007.

Ottesen, D., Dowdeswell, J.A., 2006. Assemblages of submarine landforms produced by tidewater glaciers in Svalbard. J. Geophys. Res. Earth Surf. 111 (F1). https://doi.org/10.1029/2005JF000330.

Ottesen, D., Dowdeswell, J., 2009. An inter-ice stream glaciated margin: submarine landforms and a geomorphic model based on marine-geophysical data from Svalbard. Geol. Soc. Am. Bull. 121 (11/12), 1647–1665. https://doi.org/10.1130/B26467.1.

Pearce, C., Özdemir, K.S., Forchhammer Mathiasen, R., Detlef, H., Olsen, J., 2023. The marine reservoir age of Greenland coastal waters. Geochronology 5, 451–465. https://doi.org/10.5194/gchron-5-451-2023.

Pieńkowski, A.J., England, J.H., Furze, M.F.A., Blasco, S., Mudie, P.J., MacLean, B., 2013. 11,000 yrs of environmental change in the Northwest passage: a multiproxy core record from central Parry Channel, Canadian High Arctic. Mar. Geol. 341, 68–85. https://doi.org/10.1016/j.margeo.2013.04.008.

Rantanen, M., Karpechko, A.Y., Lipponen, A., Nordling, K., Otto Hyvärinen, O., Ruosteenoja, K., Vihma, T., Laaksonen, A., 2022. The Arctic has warmed nearly four times faster than the globe since 1979. Commun. Earth Environ. 3, 168. https://doi.org/10.1038/s43247-022-00498-3.

Raymond, C.F., 1987. How do glaciers surge? A review. J. Geophys. Res. Solid Earth 92 (B9), 9121–9134. https://doi.org/10.1029/JB092iB09p09121.

RGI 7.0 Consortium, 2023. Randolph Glacier Inventory - a Dataset of Global Glacier Outlines, Version 7.0. NSIDC: National Snow and Ice Data Center, Boulder, Colorado USA. https://doi.org/10.5067/f6jmovy5navz.

Ribeiro, S., Limoges, A., Massé, G., et al., 2021. Vulnerability of the NorthWater ecosystem to climate change. Nat. Commun. 12, 4475. https://doi.org/10.1038/s41467-021-24742-0.

Robertson, S.M., 1999. Holocene Deglacial and Sea Level History of Dobbin Bay, Eastern Ellesmere Island, Arctic Canada. Master Thesis. University of Alberta, Edmonton, Alberta, Canada.

Rounce, D.R., Hock, R., Maussion, F., Hugonnet, R., Kochtitzky, W., Huss, M., Berthier, E., Brinkerhoff, D., Compagno, L., Copland, L., Farinotti, D., Menounos, B., McNabb, R.W., 2023. Global glacier change in the 21st century: every increase in temperature matters. Science 379, 78–83. https://doi.org/10.1126/science.abo1324.

Röthlisberger, H., 1972. Water pressure in intra-and subglacial channels. J. Glaciol. 11 (62), 177–203.

Ruddiman, W.F., 2001. Earth's Climate: past and Future, first ed. W.H. Freeman & Company, New York, p. 465.

Serreze, M.C., Barry, R.G., 2011. Processes and impacts of Arctic amplification: a research synthesis. Global Planet. Change 77 (1–2), 85–96. https://doi.org/10.1016/j.gloplacha.2011.03.004.

Sevestre, H., Benn, D.I., 2015. Climatic and geometric controls on the global distribution of surge-type glaciers: implications for a unifying model of surging. J. Glaciol. 61 (228), 646–662. https://doi.org/10.3189/2015JoG14J136.

Sharp, M.J., 1985. "Crevasse-fill" ridges—A landform type characteristic of surging glaciers? Geogr. Ann. 67A, 213–220. https://doi.org/10.2307/521099.

Sharp, M., Burgess, D.O., Cawkwell, F., Copland, L., Davis, J.A., Dowdeswell, E.K., Dowdeswell, J.A., Gardner, A.S., Mair, D., Wang, L., Williamson, S.N., Wolken, G.J., Wyatt, F., 2014. Remote sensing of recent glacier changes in the Canadian Arctic. In: Kargel, J.S., Leonard, G.J., Bishop, M.P., Kääb, A., Raup, B.H. (Eds.), Global Land Ice Measurements from Space. Springer Praxis Books, Springer, Berlin, Heidelberg, pp. 205–228. https://doi.org/10.1007/978-3-540-79818-7_9. Chapter 9.

Sharp, M., Burgess, D.O., Cogley, J.G., Ecclestone, M., Labine, C., Wolken, G.J., 2011. Extreme melt on Canada's Arctic ice caps in the 21st century. Geophys. Res. Lett. 38 (11). https://doi.org/10.1029/2011GL047381.

Simkins, L.M., Greenwood, S.L., Anderson, J.B., 2018. Diagnosing ice sheet grounding line stability from landform morphology. Cryosphere 12, 2707–2726. https://doi.org/10.5194/tc-12-2707-2018.

Solomina, O.N., Bradley, R.S., Hodgson, D.A., Ivy-Ochs, S., Jomelli, V., Mackintosh, A.N., Nesje, A., Owen, L.A., Wanner, H., Wiles, G.C., Young, N.E., 2015. Holocene glacier fluctuations. Quat. Sci. Rev. 111, 9–34. https://doi.org/10.1016/j.quascirev.2014.11.018.

Spagnolo, M., Clark, C.D., Ely, J.C., Stokes, C.R., Anderson, J.B., Andreassen, K., Graham, A.G.C., King, E.C., 2014. Size, shape and spatial arrangement of mega-scale glacial lineations from a large and diverse dataset. Earth Surf. Process. Landf. 39, 1432–1448. https://doi.org/10.1002/esp.3532.

Spagnolo, M., Phillips, E., Piotrowski, J.A., Rea, B.R., Clark, C.D., Stokes, C.R., Carr, S.J., Ely, J.C., Ribolini, A., Wysota, W., Szuman, I., 2016. Ice stream motion facilitated by a shallow-deforming and accreting bed. Nat. Commun. 7 (1), 10723. https://doi.org/10.1038/ncomms10723.

St-Onge, G., Mulder, T., Francus, P., Long, B., 2007. Continuous physical properties of cored marine sediments. In: Hillaire-Marcel, C., de Vernal, A. (Eds.), Proxies in Late Cenozoic Paleoceanography. *Development in Marine Geology*, vol. 1, pp. 63–98. https://doi.org/10.1016/S1572-5480(07)01007-X.

Stevenard, N., Montero-Serrano, J.C., Eynaud, F., St-Onge, G., Zaragosi, S., Copland, L., 2022. Lateglacial and Holocene sedimentary dynamics in northwestern Baffin Bay as recorded in sediment cores from Cape Norton Shaw Inlet (Nunavut, Canada). Boreas 51 (3), 532–552. https://doi.org/10.1111/bor.12575.

Straneo, F., Hamilton, G., Sutherland, D., Stearns, L.A., Davidson, F., Hammill, M.O., Stenson, G.B., Rosing-Asvid, A., 2010. Rapid circulation of warm subtropical waters in a major glacial fjord in East Greenland. Nat. Geosci. 3, 182–186. https://doi.org/10.1038/ngeo764, 2010.

Streuff, K., Forwick, M., Szczuciński, W., Andreassen, K., Ó Cofaigh, C., 2015. Submarine landform assemblages and sedimentary processes related to glacier surging in Kongsfjorden. Svalbard. Arktos 1, 1–19. https://doi.org/10.1007/s41063-015-0003-y.

Streuff, K., Ó Cofaigh, C., Wintersteller, P., 2022. GlaciDat–a GIS database of submarine glacial landforms and sediments in the Arctic. Boreas 51 (3), 517–531. https://doi.org/10.1111/bor.12577.

Syvitski, J.P.M., Stein, A.B., Andrews, J.T., Milliman, J.D., 2001. Icebergs and the sea floor of the East Greenland (Kangerlussuaq) continental margin. Arctic Antarct. Alpine Res. 33, 52–61. https://doi.org/10.1080/15230430.2001.12003404.

Tang, C.C., Ross, C.K., Yao, T., Petrie, B., DeTracey, B.M., Dunlap, E., 2004. The circulation, water masses and sea-ice of Baffin Bay. Progress in Oceanography 63 (4), 183–228. https://doi.org/10.1016/j.pocean.2004.09.005.

The GlaMBIE Team, 2025. Community estimate of global glacier mass changes from 2000 to 2023. Nature 639, 382–388. https://doi.org/10.1038/s41586-024-08545-z.

Trujillo, A.P., Thurman, H.V., 2017. Essentials of Oceanography, twelfth ed. Pearson, Boston, p. 597 (GC11.2 T78.2017).

Van Wychen, W., Burgess, D., Kochtitzky, W., Nikolic, N., Copland, L., Gray, L., 2020. RADARSAT-2 derived glacier velocities and dynamic discharge estimates for the Canadian high arctic: 2015–2020. Can. J. Rem. Sens. 46 (6), 695–714. https://doi.org/10.1080/07038992.2020.1859359.

Van Wychen, W., Halle, D.A.M., Copland, L., Gray, L., 2022. Anomalous surface elevation, velocity and area changes of Split Lake Glacier, western Prince of Wales Icefield, Canadian High Arctic. Arctic Science 8 (4), 1288–1304. https://doi.org/10.1139/as-2021-0039.

Von Grafenstein, U., Erlenkeuser, H., Müller, J., Jouzel, J., Johnsen, S., 1998. The cold event 8200 years ago documented in oxygen isotope records of precipitation in Europe and Greenland. Clim. Dyn. 14 (2), 73–81.

Woodworth-Lynas, C.M.T., Simms, A., Rendell, C.M., 1985. Iceberg grounding and scouring on the Labrador Continental Shelf. Cold Reg. Sci. Technol. 10 (2), 163–186.

Young, N.E., Briner, J.P., Miller, G.H., Lesnek, A.J., Crump, S.E., Pendleton, S.L., Schwartz, R., Schaefer, J.M., 2021. Pulsebeat of early Holocene glaciation in Baffin Bay from high-resolution beryllium-10 moraine chronologies. Quat. Sci. Rev. 270, 107179. https://doi.org/10.1016/j.quascirev.2021.107179.

Young, N.E., Briner, J.P., Miller, G.H., Lesnek, A.J., Crump, S.E., Thomas, E.K., Pendleton, S.L., Cuzzone, J., Lamp, J., Zimmerman, S., Caffee, M., Schaefer, J.M., 2020. Deglaciation of the Greenland and Laurentide ice sheets interrupted by glacier advance during abrupt coolings. Quat. Sci. Rev. 229, 106091. https://doi.org/10.1016/j.quascirev.2019.106091.

Young, N.E., Briner, J.P., Rood, D.H., Finkel, R.C., 2012. Glacier extent during the Younger Dryas and 8.2-ka event on Baffin Island, Arctic Canada. Science 337 (6100), 1330–1333. https://doi.org/10.1126/science.1222759.